ADVANCED ENERGY MATERIALS
www.advenergymat.de

Essentials of High Performance Water Electrolyzers – From Catalyst Layer Materials to Electrode Engineering

Chuyen Van Pham, Daniel Escalera-López, Karl Mayrhofer, Serhiy Cherevko, and Simon Thiele**

Proton-exchange membrane water electrolyzers (PEMWEs) will play a key role in future sustainable hydrogen production for mobility, households or chemical industry. Yet, the anode in PEMWEs, where the pivotal oxygen evolution reaction takes place, needs further improvement in terms of performance and cost. Both catalyst materials and electrode structure have to be optimized in order to inhibit degradation and reduce noble metal loadings. This review focuses on a holistic approach, covering all catalyst material, electrode structure, and transport layers within the framework of an overall electrode design, which not only optimizes the catalyst but also, all components of the electrode in conjunction. This review defines the goals for performance metrics of future PEMWEs in terms of power density and durability of the anode. Moreover, it summarizes manufacturing techniques and approaches that have a chance to be upscaled to meet the megawatt deployment of PEMWEs. The different aspects described jointly in this review such as novel catalyst system with higher intrinsic and structural performance or graded porous transport layers shall help to advance a next generation of electrodes.

1. Introduction

Over the last decades, a flourishing deployment of solar and wind power capacities has brought down the price of renewable electricity to values comparable, if not lower, than those found for electricity produced by fossil energy sources.[1] As already a large share of the direct electricity market can be covered with renewable energy, conversion, storage, and utilization also in other energy sectors becomes increasingly attractive. Moreover, due to the intermittent availability of electricity from renewable energy sources, conversion and storage is a must for effective utilization. The sustainable development of the whole energy market demanded by governmental policies (e.g., the Paris Agreement, Hydrogen strategies) and society (e.g., Friday for Future) will require new technological solutions over the next decades especially considering energy sector coupling. However, the required conversion, storage and redistribution techniques are not yet available at large scale and compatible prize. One of several ways to solve this large-scale sector coupling challenge is the conversion of excess renewable electrical energy into chemical energy of H_2 fuel (so-called green H_2) which can be stored, redistributed, and converted back to electrical power by, for example, fuel cells. Additionally, H_2 is an important feedstock in fertilizer and gas processing industry. The development of a green H_2 economy will be a key factor for the decarbonization of the future world economy, aiming to achieve a maximum global warming level below 2 °C in 2050, set by the Paris Agreement.[2,3] Water electrolysis is used to produce green H_2 from renewable energy. There are four existing water electrolysis technologies: alkaline water electrolysis (AWE); proton-exchange membrane water electrolysis (PEMWE); solid oxide water electrolysis (SOWE), and anion-exchange membrane water electrolysis (AEMWE).[4,5] The AWE type is a mature technology with the best cost-effectiveness, but has the disadvantage of comparably low current densities, high start-up times (similar to SOWE), and large system dimensions.[4] The PEMWE is the most promising type for near future large implementation given its intrinsic high power and compactness, operation capability under differential pressure with high purity of H_2 product, and especially fast response to load changes.[6] The latter is particularly important for the application using the intermittent renewable energies. AEMWE has the potential of combined advantages of PEMWE and AWE, but its deployment is still in an infancy stage due to the lack of a simultaneously sufficient conductive and stable anion-exchange membrane.[7,8]

Although PEMWE technology possesses the aforementioned advanced features, being commercialized back in 1955 by General Electric with some megawatt scale installations already being demonstrated, its widespread application is still

C. V. Pham, D. Escalera-López, K. Mayrhofer, S. Cherevko, S. Thiele
Helmholtz-Institute Erlangen-Nürnberg for Renewable Energy (IEK-11)
Forschungszentrum Jülich GmbH
Cauerstrasse 1, 91058 Erlangen, Germany
E-mail: c.pham@fz-juelich.de; si.thiele@fz-juelich.de
K. Mayrhofer, S. Thiele
Department of Chemical and Biological Engineering
Friedrich-Alexander-Universität Erlangen-Nürnberg
Cauerstrasse 1, 91058 Erlangen, Germany
The ORCID identification number(s) for the author(s) of this article can be found under https://doi.org/10.1002/aenm.202101998.

DOI: 10.1002/aenm.202101998

hindered.[9] The reason is twofold: on the one hand, high investment cost (capital expenditure, CAPEX) and on the other hand, high operating cost for H_2 production (operating expenditure, OPEX), which make the green hydrogen uncompetitive with grey H_2 (H_2 produced by reforming fossil methane).[5,10] The production cost of green H_2 in western Europe is currently in the range of 3.2–8.2 \$ kg^{-1} of H_2 compared to the 1.5–1.8 \$ kg^{-1} of grey H_2. On the other hand, green H_2 cost in Asia is projected a factor of two below that in Europe due to its abundant availability of renewable energy.[11–13] Regarding the CAPEX, at small scale, currently the main cost of PEMWE systems comes from the Ti-porous transport layers (PTL) and the bipolar plates. At larger production scales (GWs), taking into account an economy of scale effect for the bipolar plates, it is predicted that the catalyst cost will become the most significant cost factor.[9] Current PEMWEs employ high Ir loadings (>1 mg cm^{-2}) at the anodes to sustain the sluggish four-electron transfer oxygen evolution reaction (OER).[14] It has been calculated that such an extensive Ir usage would prevent the PEMWE technology deployment at the gigawatt scale due to both the scarcity and the high cost of Ir metal.[10,15] The catalyst cost has recently become an increasing factor of concern as the iridium (Ir) price has drastically increased by factor of three within the year 2020 alone. Indeed, only Ir-based catalysts fulfill the activity and stability requirements for use as anodic catalyst in PEMWEs due to the harsh anodic working conditions. In addition, the voltage efficiency of current PEMWE needs to be improved to reduce the electricity cost per kg of H_2 product, which currently accounts for 70–90% total cost.[10] These two expending obstacles could be partially overcome by developing and implementing highly efficient and stable OER catalyst layers, which can simultaneously reduce precious metal loadings, increase the longevity, and decrease the energy consumption (voltage loss) of PEMWEs.

Currently IrO_2, Ir black, and IrO_x/TiO_2 catalysts are the most successful OER catalysts for industrial PEMWEs.[16] Lessons learned from catalyst development in fuel cells, for example, that the use of carbon-supported Pt leads to an order of magnitude reduction in Pt loading, cannot directly be applied to OER catalysts. This is because the corrosive conditions within the anode of PEMWE (potential > 1.4 V and low pH) exclude the use of carbon particles as a support, since carbon corrosion theoretically occurs already at potential >0.207 V versus RHE and at a significant rate at >1.0 V versus RHE.[17–19] TiO_2 is the most promising support candidate for Ir-based OER catalysts so far, roughly corresponding to 10–30 wt% of commercial IrO_2–TiO_2 catalysts.[15] TiO_2 is specifically chosen as a support given its chemically stability against dissolution under anodic working conditions in PEMWEs.[20] Outstanding performances of PEMWEs using IrO_2–TiO_2 commercial catalysts and a Nafion 212 membrane (51 µm thick) were reported by Gasteiger et al.,[15,16] showing current density of 6 A cm^{-2} at a cell voltage of 1.92 V. However, no gas cross-over evaluation was performed in that study. Nevertheless, by thoroughly analyzing cell performance using IrO_2–TiO_2 commercial catalyst at various loadings (0.2–5.4 mgIr cm^{-2}), Gasteiger et al.[15] demonstrated that the performance of the studied cells could not meet the requirement for de-carbonization of the entire transport sector until 2100. If half of current global annual Ir supply of ≈3.6 tons would be used for PEMWEs, an Ir-specific power (Ir-SP) of ≈100 kW g_{Ir}^{-1} would be required for the de-carbonization goal. Up to now, the best power per gram ratio of IrO_2–TiO_2 commercial catalyst is ≈12.5 kW g_{Ir}^{-1} at a loading of 0.2 mg_{Ir} cm^{-2} for a cell using a 51 µm thin membrane, which is a concerning factor due to possible high gas crossover.[15] The Ir–SP is defined by Equation (1):

$$Ir-SP = \frac{i \times HHV}{2F \times l} \times 1000 \left[\frac{kW}{g}\right] \quad (1)$$

where i is the cell current density [A cm^{-2}], HHV is higher heating value of H_2 being 285796 kJ $kmol^{-1}$, F is the Faraday constant (96.5 × 106 C $kmol^{-1}$), and l is the Ir-loading (mg cm^{-2}). Babic et al.[10] made a similar analysis, but assumed H_2 as an energy vector for storage of all excess renewable energy, and ended up with the same required value of Ir–SP of ≈100 kW g_{Ir}^{-1}. If we assume that one half of both the transport sector and the energy sector could be covered by battery and other non-hydrogen storage technologies, the necessary Ir–SP to be achieved could be reduced to 50 kW g_{Ir}^{-1}. But even then, the specific performance of the aforementioned commercial catalyst is still a factor of 4 too low. The reason for this deficiency is the inefficient catalyst utilization of low loading catalyst layers (<0.5 mg_{Ir} cm^{-2}).[15,21] The resulting catalyst layers are discontinuous, partly forming electronically isolated segments, which are not connected to the Ti-based porous transport layer (PTL) due to the large pore sizes of PTLs (10–50 µm).[22] Therefore, current state-of-the-art catalysts and cell designs are not adequate for the widespread application of PEMWE with the de-carbonization goal. Significant improvement in catalyst and catalyst layer design to improve Ir–SP are needed. Future developments should focus on concerted approaches from catalyst to catalyst layer to membrane electrode assemblies (MEA) designs in order to achieve the Ir-specific power target required for large deployment of PEMWE technology. Therefore, it is necessary to understand PEMWE systems as a whole and identify the existing bottlenecks for further development. As catalyst activity and mass transport in water electrolyzers are coupled, they thus need to be jointly addressed.[23] As a prerequisite to tackle this activity transport nexus, we systematically discuss the developments from catalyst to MEA designs. In this review, we identify the most promising catalysts and MEA designs, which may enable a large-scale deployment of PEMWEs. First, the fundamentals for the development of catalyst layers are presented. Finally, the most important strategies and achievements in catalyst layer developments in terms of cell power, stability, and scale-up potential are summarized and evaluated.

2. Fundamentals for Development of PEMWE

PEMWEs are designed to enable the OER and HER to happen in two separate compartments using the electrical potential between the electrodes as the driving force, so that highly pure H_2 and O_2 can be collected. A basic design of a single PEMWE cell is shown in **Figure 1**a, which is commonly found in laboratory and industry.[9,10,15] OER and HER catalysts are coated on each side of a PEM to form an MEA. This type of MEA is called catalyst coated membrane (CCM). There are several MEA types, which will be described in the next chapter. State-of-the-art industrial PEMWEs use IrO_2 with loadings of ≈1–3 mg cm^{-2}

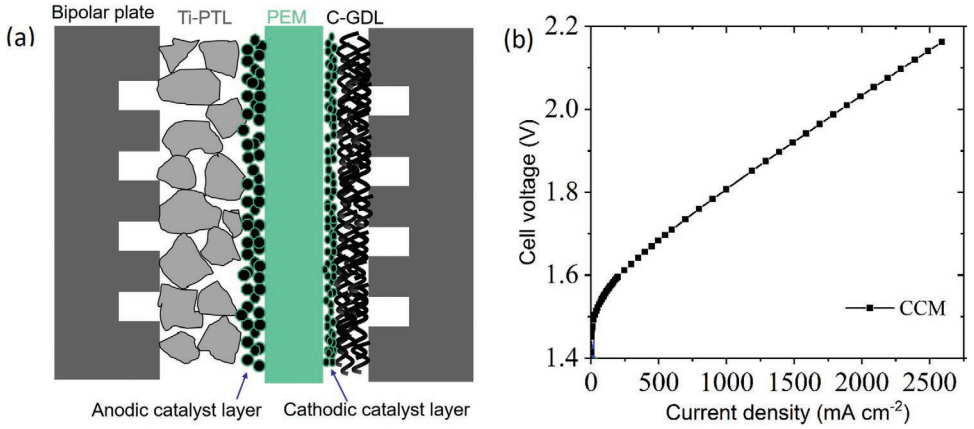

Figure 1. a) Schematic cross–section of a conventional PEMWE single cell design; b) Polarization curve of a PEMWE cell tested at 80 °C, using a CCM (FuelCellsEtc) with 1.5 mg cm^{-2} IrO_2 and 0.5 mg cm^{-2} Pt loadings on a N117 membrane.

and carbon-supported Pt nanoparticles as OER and HER catalysts, respectively.[9] Sulfonated tetrafluoroethylene based fluoropolymer-copolymers (Nafion) or perfluorosulfonic acids (PFSAs) are used as binder and proton conducting phase for both anodic and cathodic catalyst layers as well as PEM material. The PEM is electrically insulated and gas–tight to separate the produced H_2 and O_2 gases, but conducts protons to enable positive charge transfer between the electrodes independently from the electron transport. The PEM largely influences the purity of H_2 product, safety operation, and energy efficiency, which is later discussed in 4. Membrane. To facilitate the H_2O feed and the removal of gaseous products toward/from the electrode while maintaining electric contact, the MEA is compressed between a Ti-porous transport layer (PTL) at the anodic side and a C – fiber gas diffusion layer (GDL) at the cathodic side. The system is compressed and sealed by two bipolar plates (BPP), which are connected with an outer H_2O supply and product gas storage systems.

According to Faraday's law, the hydrogen production rate is directly proportional to the current density of the cell at a certain voltage. The cell power can be expressed by the cell current density at a certain voltage. Therefore, the voltage–current density relation, the so-called polarization curve shown in Figure 1b, is one of the central measures to characterize the cell conversion efficiency.

The cell voltage is composed of the thermoneutral cell voltage $U_{\text{cell}}^{\text{tn}}$ and three main overpotentials: kinetic η_{kinetic}; ohmic η_{Ω}; and mass transport η_{mt} overpotentials, which are dependent on current density and pressure as shown in **Figure 2**, according to Equation (2).

$$U_{\text{cell}} = U_{\text{cell}}^{\text{tn}} + \eta_{\text{kinetic}} + \eta_{\Omega} + \eta_{\text{mt}} \tag{2}$$

The kinetic overpotential comprises anodic and cathodic activations, $\eta_{\text{kinetic}} = \eta_{\text{kinetic}}^{\text{a}} + \eta_{\text{kinetic}}^{\text{c}}$. If the cathode employs the standard Pt/C catalyst, the kinetics of the HER is extremely fast ($\eta_{\text{kinetic}}^{\text{c}} \approx 0$), and thus cell kinetic overpotential is dominated by the anodic kinetic overpotential: $\eta_{\text{kinetic}} \approx \eta_{\text{kinetic}}^{\text{a}}$. The ohmic overpotential η_{Ω} is caused by the ionic resistance of the membrane, the electrical resistance of catalyst layers, porous transport layers and bipolar plates; and the interfacial resistances between the components in a cell. In typical cells, η_{Ω} is dominated by the ionic resistance. The interfacial resistances become significant when Ti passivation occurs during long term operation or when operating at high voltage, which is a crucial issue for practical application. Mass transport overpotential η_{mt} is caused by resistance toward fluid transport across the catalyst layer and PTL and ionic transport in the catalyst layers. The former is largely hindered by bubble accumulation at catalyst layer and PTL. The reversible cell voltage U_{cell}^{0} and U_{cell}^{tn} are calculated by Equations (3) and (4), respectively.[16,25]

$$U_{\text{cell}}^{0} = 1.2291 - 0.0008456\,(T - 298.15) \tag{3}$$

$$U_{\text{cell}}^{\text{tn}} = 1.4808 - 0.0008456\,(T - 298.15) \tag{4}$$

where T is cell operating temperature (K).

The dependence of U_{cell}^{0} and $U_{\text{cell}}^{\text{tn}}$ on pressure follows Nernst equation. The readers are referred to ref. [24] for the details of the calculations.

To minimize energy consumption, U_{cell} should be as low as possible at a specific current density. For PEMWEs, the cells

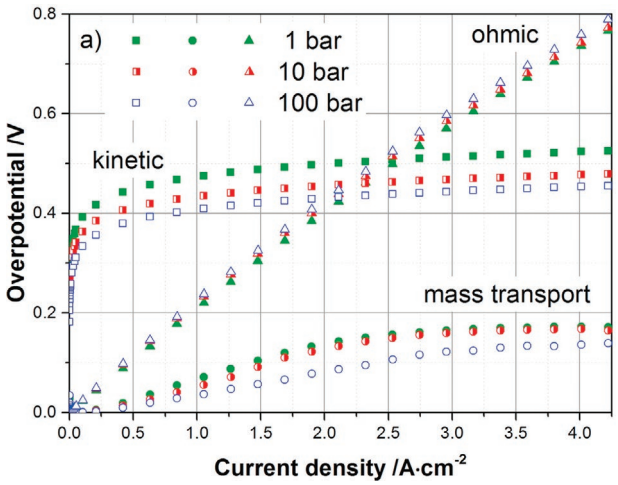

Figure 2. Overpotential (vs reversible potential) of four voltage losses in a PEMWE cell at 50 °C under different pressures. Reproduced with permission.[24] Copyright 2016, Elsevier.

Table 1. Estimated production costs of green H_2.

Year	2020			2030		
Cost	Energy cost [USD per kgH_2]	Capital cost [USD per kgH_2]	Total [USD per kgH_2]	Energy cost [USD per kgH_2]	Capital cost [USD per kgH_2]	Total [USD per kgH_2]
Case 1	1.37	1.05	2.42	1.37	0.75	2.12
Case 2	1.14	0.88	2.02	1.14	0.63	1.77

are operated at current densities approximately in the range of 1–3 A cm^{-2}. In theory, if the cell is operated at thermoneutral voltage U_{cell}^{tn} of 1.48 V and 25 °C, the minimum energy consumption for hydrogen production is 39.4 kWh kg^{-1}. Considering H_2 as an energy carrier, the energy efficiency is calculated based on U_{cell}^{tn} as Equation (5); when considering H_2 as chemical feedstock, the U_{cell}^{tn} is replaced by U_{cell}^{o} because the heat of water condensation is not useful.

$$\varepsilon = \frac{U_{cell}^{tn}}{U_{cell}} \times 100\% \tag{5}$$

Based on the PEMWE cell in Figure 1 (case 1), at 1.5 A cm^{-2} and 80 °C, the cell voltage is 1.92 V, which using Equations (4) and (5), results in $\varepsilon = 74.7\%$. At this point, the energy consumption is ≈52.7 kWh kg^{-1} of H_2. With a projected lower limit of commercial renewable energy cost of 0.026 USD per KWh,[26] the energy cost alone is 1.37 USD per kgH_2. The same calculation can be done for one of the best reported PEMWEs (case 2).[15] Here, the cell voltage is 1.6 V (ε_{HHV} = 89.6%) at 1.5 A cm^{-2}, and the energy consumption is ≈44.0 kWh kgH_2^{-1}, corresponding to 1.14 USD per kgH_2. Both ref. [10] and an expert elicitation study[4] projected an average capital cost corresponding to ≈1200 USD per kW of installed power PEMWE and average lifetime of 60 000 h for year 2020, and 1000 USD per kW and 70 000 h for year 2030. Based on these numbers, we calculated the CAPEX cost per kg H_2 by dividing the total energy input during the lifetime by the energy consumed to produce 1 kg H_2 for the two cases aforementioned. The results are shown in **Table 1**.

The estimated results of hydrogen production costs are between 2.02 and 2.42 USD per kgH_2 for the year 2020 and 1.77–2.12 USD per kgH_2 for the year 2030, based on the two examples. The lower value of the case 2 for the year 2020 might become competitive with the cost of grey H_2 if CO_2 tax is added, and for the year 2030 estimations, it is comparable with the current cost of grey H_2. Based on such rough estimation at the single cell level, boundary parameters for cell development and components can be derived. Gas post-compression energy cost and other system energy loss are excluded. From the economic standpoint, PEMWEs can only penetrate the market at GW scales, if they can produce cost-effective green H_2. Thus, the PEMWE should be operated ideally at voltages ≤1.6 V (as in case 2). From this estimation and the limited Ir resource analysis mentioned in the introduction,[10,14,15] and the target of operation durability adopted by DOE,[27] we outline the targeted parameters of PEMWEs for future developments toward widespread application (GW scales) in **Table 2**.

Table 2. Critical parameters for enabling widespread application of PEMWEs.

Cell activity at 1.6 V	Ir–PD at 1.6 V	Degradation rate [DOE target][27]
≥1.0 A cm^{-2}	≥50 kW g_{Ir}^{-1}	≤6 µV h^{-1}

2.1. Thermodynamics and Kinetics of Water Splitting Reaction

Green hydrogen can be produced via the water splitting reaction (R3). In PEM electrolysis, this reaction is separated into two half-cell reactions:

$$2H_2O \rightarrow O_2 + 4H^+ + 4e^- \text{ at the anode} \tag{R1}$$

$$4H^+ + 4e^- = 2H_2 \text{ at the cathode} \tag{R2}$$

The sum of [R1] – oxygen evolution reaction (OER) and [R2] – hydrogen evolution reaction (HER) results in overall reaction [R3].

$$H_2O \rightarrow \frac{1}{2}O_2 + 2H_2 \tag{R3}$$

Electric energy is provided for reaction [R3] that equals the reaction enthalpy, which includes the reactions free energy and heat needed to account for the entropic change within the system.

$$\Delta W_e = \Delta H^\circ = \Delta G^\circ + T\Delta S^\circ \tag{6}$$

where ΔW_e, ΔH°, ΔG°, and ΔS° are electrical energy, reaction enthalpy, free energy and entropy, respectively.

If reaction [R3] occurs at standard condition (25 °C, 1 bar) and the heat for entropy change is provided externally, ΔW_e equals ΔG° = 237 kJ mol^{-1}. This requires a minimum cell voltage U_{cell}^{o} of 1.23 V, which is corresponding to the so called reversible potential of the reaction [R3]. In low temperature electrolysis systems operated in the range of 60–90 °C, all energy is provided by an electric source, thus ΔW_e equals $\Delta H^\circ = \Delta G^\circ + T\Delta S^\circ$ = 286 kJ mol^{-1}. Therefore, a minimum potential U_{cell}^{tn} of 1.48 V is required for reaction [R3] to happen at standard conditions, which is called thermoneutral voltage. As soon as a current is drawn during PEMWE operation, the cell voltage is higher than U_{cell}^{tn} of 1.48 V due to the voltage loss mechanisms, as previously presented in Equation (2). Kinetic losses include the required overpotentials to drive the reactions [R1] and [R2]. To reduce the kinetic overpotentials, finding

better catalysts is one of the central approaches. Another way to mitigate kinetic losses is the catalyst layer design, which is discussed later. Under acidic conditions, the kinetics of HER on Pt catalyst are extremely fast, occurring with negligible overpotential. The adsorption of hydrogen atoms on the catalyst surface is crucial for the HER kinetics, and the free binding energy of hydrogen adsorption (ΔG_H) is known to be the most important descriptor besides the water–catalyst surface interaction.[28] Pt is known to be the best catalyst for the HER with a ΔG_H of ≈0. With a four proton-coupled electron transfer (PCET), the OER, reaction [R1], is more complex than the HER and takes place through multistep reactions; as it requires high overpotentials, it accounts for one of the major voltage losses of PEMWE.

The apparent current density exponentially scales with overpotential (η_{OER}) applied, according to Tafel Equation (7a,b).

$$\eta_{OER} = \frac{2.303RT}{\alpha_a F}\log\left(\frac{i}{i_0}\right) = b\log\left(\frac{i}{i_0}\right) \tag{7a}$$

or

$$\frac{i}{i_0} = 10^{\frac{\eta OER}{b}} \tag{7b}$$

where R is the universal gas constant, α_a the anodic transfer coefficient, $\frac{2.303\,RT}{\alpha_a F} = b$ the Tafel slope.

The Tafel slope b is an important metric to evaluate the activity of a ORR catalyst. According to Equation (7a,b), if the i_0 is constant, the smaller the value of b is, the better the activity of the catalyst. The Tafel slope b can be experimentally determined by plotting the linear relationship between the potential (in half-cell) or voltage (in full cell) and the logarithm of the current density, the so called Tafel plot. b is the slope of the plotting line versus the x-axis with the unit of mV per decade (mV dec^{-1}). The rutile IrO_2 OER catalyst typically presents values of b ranging between 45 and 60 mV dec^{-1}.[16,29]

The next section will highlight recent developments and identify the most promising approaches toward meeting the critical target parameters for catalyst activity and stability in PEMWEs from Table 2. As discussed earlier, the kinetics of the HER at the cathode are extremely fast, having little influence on the overall cell performance. Therefore, the next sections will focus on the development on the anodic catalyst layers as the largest research topic in electrocatalysis for PEMWE technology.

3. Anodic Catalyst Layer Development

3.1. Catalyst Synthesis Methods

As the OER occurs at high overpotential compared to the thermodynamically defined base voltage, the deployment of high performing catalysts at the anodes is of utmost importance to enable energy-efficient operation (low voltage) of a PEMWE. Due to the harsh anodic working conditions (high voltage in acidic medium), only Ir based catalysts have been demonstrated so far to fulfill the stability requirements for use in PEMWEs as described in Table 2. Therefore, this section focuses on the development of Ir and Ir/Ru alloy based catalysts. With respect to practical applications, we concentrate on methods which can produce significant catalyst amounts for electrode fabrication as only those methods will have a chance to make a contribution for commercial systems. An overview of the focused methods with reaction parameters is summarized in **Table 3**.

3.1.1. Adam's Fusion Method

The Adam's fusion method was first introduced by Adam and Shriner for the synthesis of PtO_2.[30] It was then applied to IrO_x and $Ir_xRu_{1-x}O_2$ catalysts, and became a widely used method for the synthesis of these catalysts.[31,32] It is a simple method based on two steps. In the first step, Ir and Ru precursors are mixed with $NaNO_3$ in a solvent solution by stirring at room temperature, followed by solvent evaporation to dryness (R4). TiO_2 particles can be added in this step to synthesize support catalyst. In the second step, the fusion reaction is performed, manifesting in the chemical reaction (R5). The fusion reaction (R5) is often performed by heating in air at temperatures of ≈500 °C. A final washing step is applied to obtain pure IrO_2. $Ir_xRu_{1-x}O_2$ catalysts can also be synthesized by this method by using a mixture of Ir and Ru precursors salts in the first step.[32] The Adam's fusion method is often used to synthesize highly crystalline catalysts as it takes place at temperature as high as 500 °C.

$$H_2IrCl_6 + 6NaNO_3 \rightarrow 6NaCl + Ir(NO_3)_4 + 2HNO_3 \tag{R4}$$

$$Ir(NO_3)_4 \rightarrow IrO_2 + 4NO_2 + O_2 \tag{R5}$$

Table 3. Overview of the synthetic methods with reaction parameters.

Methods	Precursors	Reactants	Calcination T °C	Supported catalysts possible	Crystallinity
Adam's fusion	H_2IrCl_6, H_2RuCl_6 or hydrate $IrCl_3$ and $RuCl_3$	$NaNO_3$	400–500	Yes	High
Pechini–Adams	Hydrate $IrCl_3$ and $RuCl_3$,	Polymers, Air–O_2	400–500	Yes	High
Hydrothermal	Hydrate $IrCl_3$ and $RuCl_3$	LiOH or NH_3	250–500	Yes	Low–high
Polyol methods	H_2IrCl_6, $IrCl_3$ or $RuCl_3$	NaOH	Hydrolysis in ethylene glycol	Yes	Low
Reactive spray deposition	Iridium acetylacetonate	Dethylene glycol monobutyl ether, ethanol, xylene, air–O_2	1700–2000	Yes	High

3.1.2. Modified Adams Methods

This group of methods is based on thermal decomposition of Ir or mixed Ir/Ru precursors under oxygen atmosphere without adding the nitrate oxidant as in the original Adam's fusion method. For example, $RuCl_3$ and $IrCl_3$ are included in a polymerization process by adding $RuCl_3$ and $IrCl_3$ in HCl acidic solution to a solution of citric acid in ethylene glycol, followed by stirring under raised temperature of 90 °C. Under this condition, polymerization occurs to form a metal polymeric precursor. In the next step, the metal polymeric precursor is calcined at temperatures of up to 400 °C under oxygen atmosphere to decompose the composite and to produce IrO_x or $Ir_xRu_{1-x}O_2$ particles. Herein, reactions (R6 and R7) occur.[33] This method with polymeric precursor is called Pechini–Adams method.

$$2IrCl_3 + 2O_2 \rightarrow 2IrO_2 + 3Cl_2 \quad \text{(R6)}$$

$$2RuCl_3 + 2O_2 \rightarrow 2RuO_2 + 3Cl_2 \quad \text{(R7)}$$

3.1.3. Hydrothermal Methods

This method comprises two steps:[34,35] To start, Ir or Ir/Ru mixed salts, for example, $IrCl_3$, $RuCl_3$ react with hydroxyl, for example, LiOH or ammonia to form the precipitate of $Ir(OH)_3$ or $Ir_xRu_{1-x}(OH)_3$. TiO_2 particles can be added in this step to synthesize support catalyst. In the next step, the intermediates $Ir(OH)_3$ or $Ir_xRu_{1-x}(OH)_3$ are calcined at various temperatures (250–500 °C) to produce the oxide form of IrO_x and $Ir_xRu_{1-x}O_y$ catalysts with different crystallinities. The higher the temperature applied, the higher the degree of crystallinity of the catalyst products that is obtained. Therefore, this method can be used to synthesize amorphous IrO_x and $Ir_xRu_{1-x}O_y$ catalysts, which are known to have higher activity but are less stable toward OER than crystalline IrO_2 and $Ir_xRu_{1-x}O_2$ catalysts.

3.1.4. Polyol Methods

This method has the same starting step as the hydrothermal methods. Contrary to those methods, however, the polyol methods use high boiling point solvents such as ethylene glycol to hydrolyze the intermediate $Ir(OH)_3$ or $Ir_xRu_{1-x}(OH)_3$ into IrO_x and $Ir_xRu_{1-x}O_y$ particles, respectively in solution at high temperature, for example, 175 °C.[36] Ir or Ru salts such as H_2IrCl_6, $IrCl_3$ or $RuCl_3$ are often used as metal precursors. NaOH is added to form and precipitate the intermediates. Ethylene glycol acts as both solvent and ligand for constraining the particle size to grow. The catalyst support such as TiO_2 can be added to the reaction solution to synthesize supported catalysts.

3.1.5. Reactive Spray Deposition Technology

Reactive spray deposition technology (RSDT) was used to produce various nanoparticles, for example, Pt nanoparticles as a fuel cell catalyst.[37] This method was recently applied to synthesize IrO_x nanoparticles, which were directly coated onto the membrane to form catalyst layers in an additional coating step.[38] The method was more recently also used to synthesized various $Ir_xRu_{1-x}O_2$ alloy catalysts.[39,40] Iridium acetylacetonate as Ir precursor is dissolved in mixed solvents of diethylene glycol monobutyl–ether, ethanol, and xylene with 1: 1: 2 vol. ratio. The solution precursor is then mixed with 16 wt% propane, before being sprayed through an atomizing nozzle, and burned under a flame at high temperature of 1700–2000 °C. Under this high temperature, the IrO_x particles are formed and calcined, then immediately cooled down by an air-quenching step. During the flight, the IrO_x particles are mixed with Nafion solution in a second nozzle before being sprayed on the Nafion membrane substrate. This method can produce a high performing catalyst layer with loading as low as 0.08 mg cm^{-2},[38] but requires unique and rather advanced apparatus.

3.2. Evaluation of Catalyst Activity and Stability

3.2.1. Fundamental Catalyst Testing With Classical Electrochemical Techniques

Before testing in a PEMWE configuration, the activity evaluation of any oxygen evolution electrocatalyst relies on rotating disk electrode (RDE) experiments in a three-electrode cell configuration. In brief, catalyst thin films are prepared onto an RDE tip of a well-defined geometric area by drop casting catalyst ink suspensions, followed by potentiodynamic polarization to OER potentials using linear sweep voltammetry (LSV) or cyclic voltammetry (CV) in an aqueous acidic electrolyte (0.1 M $HClO_4$ or 0.5 M H_2SO_4). This was adopted from previous research on fuel cell electrocatalysis, where thin film RDE (TF-RDE) testing proved that relevant kinetic parameters can be extracted from nanoparticulate catalysts for hydrogen oxidation[41] and oxygen reduction reactions.[42] In order to benchmark the performance of different electrocatalysts, several activity benchmarking metrics have been traditionally proposed: Tafel slope analysis, η_{OER} at a given geometric current density j_{OER} (0.5 or 10 mA cm^{-2}),[43] or experimental j_{OER} at a given OER potential (1.55 or 1.6 V_{RHE}).[44] Tafel slope analysis, as shown in Section 2, is employed to ascribe the rate-determining OER reaction step, but also provides a metric of the electrocatalyst efficiency: the required η_{OER} (energy input) to achieve an order of magnitude increase in j_{OER}. Therefore, low Tafel slope values are desirable to drive OER electrocatalysis. Tafel plot analysis, however, should be carefully performed given the potential-dependent slope values on most OER catalysts.[29] Indeed, exchange current densities (j_{OER} at $\eta_{OER} = 0$) cannot be reliably extracted as the extrapolation from high η_{OER} to reversible potential values does not take into consideration that rate-limiting steps present a potential dependence.[45,46] Other factors limit the reliability of Tafel analysis from LSV/CV: the potentiodynamic nature of LSV/CV, uncompensated ohmic resistance (R_U), and bubble accumulation. When compared to steady-state potential/current plots obtained by chronopotentiometry (CP) or chronoamperometry (CA), Tafel slopes from LSV/CV were shown to deviate from their true value, worsening if ohmic compensation is

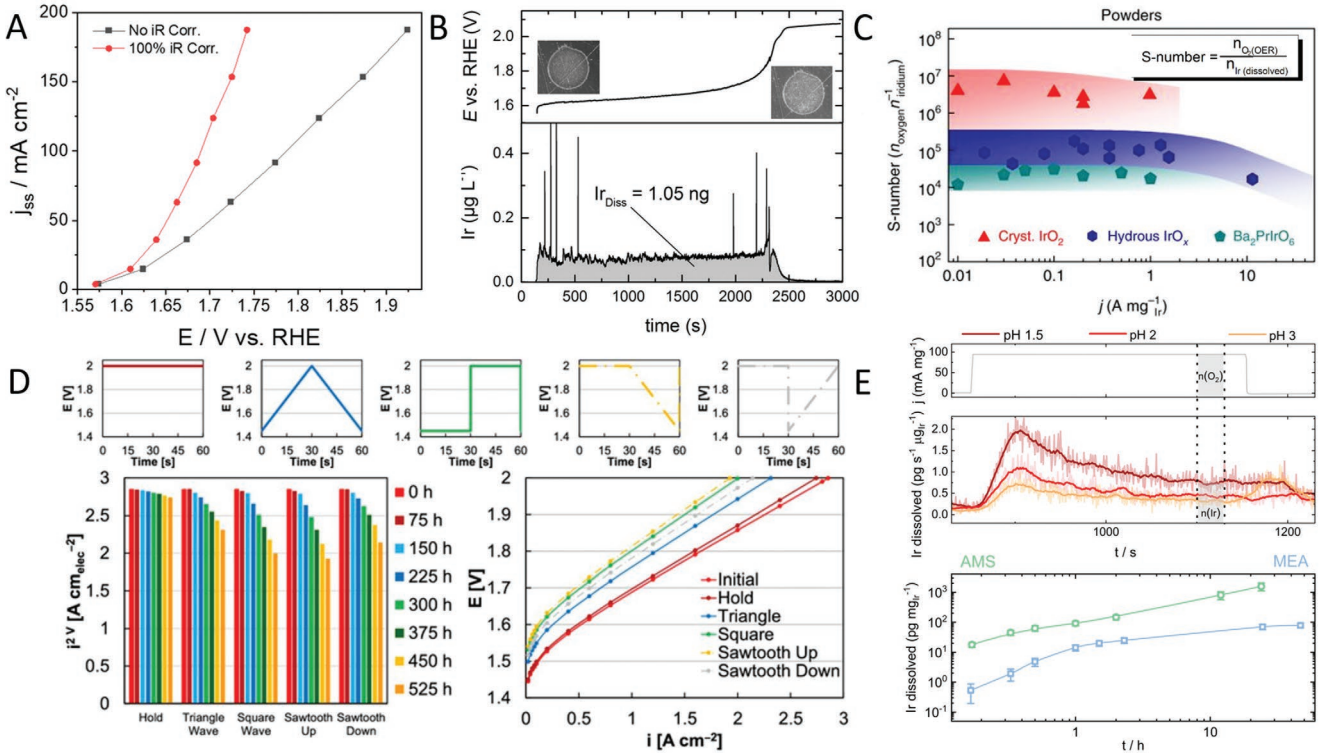

Figure 3. A) Steady-state current density values obtained during CA measurements, and the impact of *iR* compensation (100%) in experimental curves: before (black), and after (red). Reproduced with permission.[47] Copyright 2021, American Chemical Society. B) Time-dependent evolution of experimental OER potential during 0.5 A mg_{Ir}^{-1} CP hold on a metallic Ir catalyst drop casted on glassy carbon electrode (top), and the Ir dissolution profile simultaneously recorded (bottom). Reproduced with permission.[54] Copyright 2017, Wiley-VCH. C) S-number plotted versus mass-specific Ir current densities for IrO_2 (red), hydrous IrO_x (blue), and an Ir-based perovskite (green). Adapted with permission.[55] Copyright 2018, Springer Nature. D) Alternative AST profiles employed for MEA testing: potential hold, triangle-wave, square-wave, upward sawtooth, and downward sawtooth (top). AST profile-dependent MEA currents recorded at 2 V between 0 and 525 h of operation (bottom left) and the corresponding polarization curves before (red) and after 525 h operation (bottom right, see label insets). Reproduced with permission.[56] Copyright 2019, The Authors. E) Variation of the dissolution profiles of a commercial IrO_x catalyst with respect to the electrolyte pH (top). Discrepancy in the long-term stability of IrO_x in MEA (blue) and aqueous model system (AMS, green), normalized by Ir loading: 2 A mg_{Ir}^{-1} and 0.2 A mg_{Ir}^{-1}. Adapted with permission under the terms of the Creative Commons CC BY license.[57] Copyright 2021, the Authors. Published by Springer Nature.

not applied (**Figure 3**A).[47] This was ascribed to interferences from double-layer charging and catalyst's self-oxidation, which are aggravated at scan rates higher than 0.1 mV s^{-1}. Misleading Tafel slopes were also found for poorly-conducting electrocatalysts, where high ohmic resistances decreased catalyst utilization (i.e., catalyst areas electrically connected to the backing electrode), resulting in Tafel slopes higher than those intrinsic of the electrocatalysts.[48] Even after accounting for R_U, its value under OER operation is affected by O_2 bubble formation: accumulation of a non-conducting gas phase not only blocks active sites but also increases the experimental value of R_U, increasing the uncertainties of ohmic compensation during OER testing.[49] Similarly, metrics related to j_{OER} preclude clear comparisons, given that important parameters such as catalyst loading, porosity, and active surface area are not accounted for. Instead, mass or surface-specific activity metrics normalized by the ECSA provide a better comparability across studies.[50] For Ir-based metal oxides, however, ECSA elucidation is not a trivial endeavor as the recently proposed techniques employ toxic reagents (mercury underpotential deposition)[51] or challenging interpretation (electrochemical impedance spectroscopy).[52,53]

Electrochemical stability of OER catalysts is generally evaluated by long-term CP or CA measurements (2 to 24 h at 10–20 mA cm^{-2}),[58] where the initial and final j_{OER} or η_{OER} are compared: minor modifications in these metrics are then related to high electrocatalyst stabilities. However, evaluation of these alone does not provide a comprehensive picture, as they solely focus on electrochemical metrics (time-dependent loss of electrocatalytic performance) instead of catalyst metrics (time-dependent catalyst loss or surface restructuring). Indeed, any η_{OER} increase when performing CP measurements, assuming that both catalyst OER kinetics and roughness factors are not modified during operation (i.e., constant Tafel slope), should be consistent with the Tafel Equation (7a). As an example, if η_{OER} increase is three times the Tafel slope of the studied electrocatalyst, this would indicate that only 0.1% of the initial ECSA would still be available to drive OER catalysis, that is, a 99.9% of catalyst performance loss. Nevertheless, such experimental OER potential η_{OER} increase can be driven by catalyst degradation, but also by oxygen micro-bubble accumulation at the catalyst layer. The latter is a clear example of the misguiding physical relevance of such electrochemical metrics: as oxygen

micro-bubbles block the surface of undegraded OER active sites, their macroscopic effect in the OER potential would indicate an irreversible catalyst loss. El-Sayed and co-workers explored the effect of such measurement artefact and showcased that, during CP holds performed with a TF-RDE setup under forced convection, only oxygen macro-bubbles could be effectively removed from the catalyst layer surface. The remaining nano- and micro-bubbles present at the catalyst porous structure, partially responsible for the η_{OER} increase, could only be removed by argon purging at OCP after OER testing[59] or ultrahorn sonication during OER operation.[60] Both approaches effectively recovered the catalyst OER activity, although not fully due to catalyst degradation taking place. A later study suggested that, if not removed, such microscopic bubbles could even induce irreversible catalyst degradation.[61] The most recent hypothesis behind micro-bubble accumulation in a TF-RDE catalyst layer is the lack of a downward oxygen pressure gradient across the catalyst layer cross-section, which prevents microbubble removal based on RDE convection lines.[61]

To unambiguously report stability metrics, offline and/or coupled analytical techniques such as electrochemical quartz crystal microbalance or inductively-coupled plasma mass spectrometry (ICP-MS) should be employed, as they allow a direct correlation between electrochemical performance decay with catalyst losses.[62,63] A valuable experiment by Geiger et al. showcased this need: a scanning flow cell (SFC) with on-line analytics (ICP-MS) was used to monitor the dissolution rate of a commercial metallic Ir catalyst, showing that the increase in experimental OER potential observed (up to ≈2.2 V_{RHE}) was not related to Ir catalyst loss but to the passivation of the glassy carbon backing electrode employed (Figure 3B).[54] The question then arises as to whether the stability metrics stemming from classical electrochemical systems are comparable across laboratories and, if so, to which degree these are representative of catalyst layer degradation in PEMWE environments.

To provide a better framework for catalyst stability benchmarking, a recent study proposed a new metric: the stability number (S-number).[55] This metric normalizes the amount of oxygen evolved by the electrocatalyst (assuming a 100% Faradaic efficiency conversion of anodic integrated current) by the amount of dissolved Ir, quantified by integrating the dissolution profiles during SFC-ICP-MS measurements. The metric robustness was evaluated by benchmarking several Ir-based catalysts (metallic Ir, rutile-type IrO_2, hydrous IrO_x, Ir-based perovskite) at varying mass-normalized OER current loads. For each material tested, S-numbers remained constant, indicating a clear correlation between OER currents and dissolution rates (Figure 3C). The S-number metric has been successfully employed in various studies,[39,64–70] proving to yield comparable values across laboratories for given catalysts.

Using electrochemical metrics alone, Alia and co-workers showed that OER durability is in stark discrepancy between RDE and PEMWE systems, especially for metallic Ir catalysts. Employing potentiostatic holds at 2 V, it was shown that catalyst activity was fully lost in RDE in less than 6 h, whereas for MEA performance, it was maintained for ≥2 weeks at lower degradation rates.[71] To further corroborate such discrepancy, the S-number metric was used to compare the expected lifetimes of a RuO_2 catalyst under SFC-ICP-MS and PEMWE operation. It was shown that PEMWE lifetimes were two orders of magnitude higher, indicating that classical electrochemical systems clearly underestimate stability metrics. Additional experiments by Cherevko and co-workers on a metal-free custom made MEA setup showed that the higher catalyst stabilities in PEMWE environments have two main contributors (Figure 3E).[57] First, a higher local pH at the catalyst layer interface (2–3) than the one assumed in contact with the strong acid sulfonated groups in Nafion membranes (pH ≈ 0). Second, the extended operational timescales of PEMWEs, which grant an additional stabilization pathway still to be fully uncovered. Indeed, many factors play a role in the limitations of classical electrochemical systems as stability descriptor tools. These are mainly (but not limited to) intrinsic differences in the electrode architecture and operational parameters of aqueous model systems versus PEMWE devices, which are beyond the scope of this work but critically analyzed in our recent mini-review.[72]

3.2.2. Catalyst Performance and Degradation in MEA Systems

The activity and durability of PEMWE setups is generally assessed by electrochemical metrics. For activity, the cell voltage attains current densities of 1–2 A cm^{-2} during acquisition of *I–V* polarization curves after an activation protocol. For durability, galvanostatic holds at similar current densities (1 A cm^{-2} being more widespread) are exerted to evaluate short-term (10–24 h) and long-term (100–1000 h) degradation under constant operation, reported with respect to voltage losses in μV h^{-1} or mV h^{-1}. During activity measurements, kinetic parameters such as Tafel slopes and exchange current densities can be investigated. These are generally assessed at a small current density range (0.01 to 0.1 A cm^{-2}), where mass transport losses are assumed to be negligible.[73] In such measurements, ohmic drop correction must be accounted for by electrochemical impedance spectroscopy (EIS) measurements, to elucidate HFR values and truly extract kinetic-dependent parameters. Given the fast kinetics of the quasi-reversible HER and their negligible contribution to the total cell overpotential (Section 2), a generalized assumption is that the extracted kinetic parameters directly correspond to those of the sluggish OER (see Section 2).[74] Surprisingly, a cross-laboratory study reported by Bender and co-workers showed that the 1 A cm^{-2} performance metric across the PEMWE literature reviewed presented a discrepancy of 200–600 mV, less severe for thicker membranes (Nafion 117).[75] From their study, they showcased that accuracy in cell temperature control (3–4 mV loss per °C of temperature decrease) along with the completeness of the conditioning protocol, which is generally user-dependent, were the major drivers in the results variability.

In terms of durability, the aforementioned testing timescales are far from the expected lifetimes of commercial PEMWEs (>50 000 h),[9] and the fluctuating conditions under which PEMWEs would operate when coupled to renewable energy sources. Unlike the fuel cell community, there is yet no consensus on standard testing protocols to report PEMWE durability targets such as the ones proposed in Table 2 (Section 2.1), especially under dynamic operation. To obtain reliable degradation metrics at shorter timescales, several accelerated stress

tests (AST) were suggested,[76] and discussed elsewhere.[77] A study by Alia and co-workers aimed to adapt the extracted energy inputs from wind and solar energy profiles in a testing protocol, and compare the obtained degradation rates with MEAs operated under square-wave or triangle-wave operation (voltage cycled between 1.4 and 2.25 V).[56] It was shown that performance loss under renewable degradation was 2–3 times lower than with the wave stressors used (Figure 3D). This was related to the higher frequency of cycling between no operation (1.4 V) and high operation (2.25 V) when using AST stressors: once per minute instead of once per day for renewable energy profiles. This suggests that a fine-tuned AST protocol can provide meaningful information on realistic catalyst layer lifetimes.

Other relevant factors coming into play when studying PEMWE cell degradation are the anode catalyst loadings and, if operated under non-dynamic conditions, the cell current densities employed during degradation protocols. There is a general consensus in the literature that unsupported IrO_2 catalyst loadings < 0.5 mg_{Ir} cm^{-2} yield inhomogeneous catalyst layers, where the lack of a percolated electrical pathway across NPs and the membrane yields an increase in the overall cell voltage of 100–150 mV when decreasing the loadings to 0.1 mg_{Ir} cm^{-2}.[78] For a given catalyst layer, parameters such as the water flow rate and the PTL porosity notably change the obtained cell performance, with a higher sensitivity at lower Ir catalyst loadings.[79] Conversely, higher loadings yielding thicker catalyst layers (>5–10 μm, >1.5 mg_{Ir} cm^{-2}) result in cell voltage increases due to mass transport resistances, even when IrO_2 was more evenly distributed across a percolated network of TiO_2 support.[15,80] Long-term degradation studies suggest, at a given current density and at equivalent operating conditions, that lower loadings yield faster degradation rates. Maric and co-workers, after reviewing the literature, established a general trend: PEMWE cells prepared with Ir/IrO_2 loadings lower than 1 mg cm^{-2} presented degradation rates > 100 μV h^{-1}, which are <100 μV h^{-1} if current density operation values are lower (0.5–1 A cm^{-2}).[38] It is noteworthy to point out, though, that more advanced anode catalyst layers present degradation rates of 10–20 μV h^{-1} at currents higher than 1 A cm^{-2}.[81,82]

On the other hand, higher degradation is generally observed in PEMWE cells when operated at higher current densities at a given catalyst loading. Siracusano et al. evaluated further the origin of such trends employing an $Ir_{0.7}Ru_{0.3}O_2$ anode electrocatalyst, reporting that cell voltage degradation was threefold higher (15 μV h^{-1} vs 5 μV h^{-1}) when the operating current was modified from 1 to 3 A cm^{-2} during 1000 h of operation. Indeed, they identified a direct correlation between PEMWE degradation rates and both the catalyst turnover frequencies and the thermal power production. This indicated that catalyst degradation was directly correlated with faster OER rates and local heat which could cause catalyst dissolution and sintering, among other phenomena.[82] Stability studies of IrO_2 electrocatalysts with the SFC-ICP-MS setup suggest that Ir dissolution is only prominent at anode potentials ≥ 1.6 V.[83,84] As shown by Maric and co-workers, this is the case for anodes with ultra-low loading (0.08 mg_{Ir} cm^{-2}), where anode potentials are ≈1.9–2 V and Ir dissolution accounts for 42% of the anode catalyst loss after 4500 h operation at 1.8 A cm^{-2}.[85]

Regardless of the testing protocol and catalyst loading, any PEMWE degradation metric is the net result of degradation phenomena across each component, not just the catalyst layer. As an illustrative example, for a single cell run for 1000 h at 2 A cm^{-2}, it was estimated that 78% of the recorded losses were allocated to ohmic resistance losses at the anodic Ti PTL due to surface oxidation.[86] Indeed, EIS measurements at different current densities during PEMWE operation were already used to decouple overpotential losses during degradation arising from kinetic, ohmic, and mass transport effects.[73] For further information, we refer the reader to a recent review breaking down the degradation mechanisms of PEMWE components during operation,[87] and another one devoted to the critical areas involved in PEMWE degradation.[10]

Evaluation of the catalyst layer degradation is normally limited to post-mortem characterization techniques to evaluate changes in morphology and thickness (SEM), crystallinity of the catalyst structure (XRD, TEM), and composition (EDX, XPS, XRF) within the catalyst layer or across the MEA and its constituents. As a representative example, Hartig-Weiss et al. showed that, under OCV recorded during intermittent operation, hydrogen crossover at 80 °C from the cathode reduced IrO_2 to metallic Ir. Using EDX and SEM cross-section analysis, it was shown that under OER potentials, this further re-oxidized to the highly-active yet unstable hydrous IrO_x, which dissolved and migrated to the membrane.[88] Further information on the benefits of each characterization technique can be found in other works.[58]

In order to decouple the contributors to performance losses, and provide a more realistic picture of the degradation phenomena involved, in situ and in operando studies are paramount as shown for OER model systems.[89–91] A recent study from Kang et al. used gold ribbon sense wires to measure though-plane voltage losses under cell operation.[92] These confirmed that CCMs, specifically the CL/PTL interfacial contact resistance, have the highest contribution in high-frequency resistance losses: 100-fold than that of anode and cathode current collectors. During long-term operation testing, experimental resistance at the cathode remained constant, which for the case of the anode was only observed when the PTL was Ir-coated. Similarly, Hinds and co-workers reported a modified PEMWE setup which included a reference electrode externally coupled via a salt bridge.[93] Initially employed to decouple anode and cathode voltage contributions, this was recently employed to monitor corrosion potentials in anode current collector[94] and Pt dissolution at the cathode under OCV conditions.[95] These methods, if adapted, could potentially be used to track down anode catalyst layer degradation. Indeed, ICP-MS measurements on MEA anode catalyst layers were already reported.[96] But it is only meaningful if minimum metal components are used, so that galvanic redeposition of Ir is avoided. If redeposition occurs, Ir dissolution rates decrease with PEMWE operation time, instead of increasing up to a stable value in the metal-free MEA setup (Figure 3E).[57]

3.3. Electrode Development

The performance of PEMWEs cells with respect to electrodes is usually evaluated with three main parameters: hydrogen

conversion efficiency, hydrogen produced per cell unit area, and operation durability. Anodic catalyst layers are designed to enable the OER, reaction [R1], to take place at the highest kinetic rate possible. Overall, the reaction requires the supply of H_2O and electrons to the catalyst surface as well as fast removal and transport of the products O_2 and proton to successively free the reaction surface for more reactants. Due to the reactants and their transport pathways, the OER occurs at interfaces of three different phases at the catalyst surface. The electron-conducting phase is formed by the (supported) catalysts, Ti-fibers of the PTL (electron transport factor), and the current collectors. The proton-conducting phase is created by the ionomer within the catalyst layer in connection with the PEM and to some extent by the liquid water. The mass-transport phase is formed by the percolating pores of the catalyst layer and the pores of the PTL. Any limitation in one of the three transport phases will lead to a higher overpotential, and therefore to a higher cell operation voltage (corresponding to Equation (2)). The target design therefore is to create catalyst layers with the highest possible interfacial area in the catalyst layer, while providing the shortest possible mass transport toward the reactive centers. In nature, an example of solving this challenge is a tree, which efficiently transports all needed nutrients via the trunk and branches to the leafs. In trees, the venation pathway from the trunk via the increasingly smaller branches toward the leafs conforms a hierarchic, graded transport structure. "Hierarchic" implies that there are features on different length scales important for the functionality of the structure, whereas "graded" indicates that these length scales become increasingly smaller in one direction as illustrated in **Figure 4**. Likewise, electrodes from the transport channels in the bipolar plates, over porous transport layers to the catalyst layers form a hierarchic, graded pore and solid network with decreasing pore sizes and increasing surface area per volume. This enables fast mass and electron transport processes through the pores and solid parts, respectively, toward the nanometer scaled catalyst layers. One parameter to evaluate the surface area is the ECSA of a catalyst layer. High ECSA, while maintaining the three transport factors at optimum values is an angular cornerstone in catalyst layer and electrode design. Porous catalyst layers are usually obtained by first mixing nanostructured IrO_2 catalyst particles with ionomer solution in a solvent to form a catalyst ink, followed by a layer formation process via applying coating techniques such as spray coating, knife-coating or slot-die coating. The thicknesses of catalyst layers are typically of 3–10 µm for noble metal catalysts. They are usually not self-standing, but typically adhere to a mechanically stable cell component which is either the PEM or the PTL. These two options, PEM or PTL result into the two main MEA configurations: catalyst coated membrane (CCM) and catalyst coated porous transport layers which are well-known as porous transport electrodes (PTEs). These two basic configurations (CCM or PTE) give rise to different manufacturing and thus structuring options which are discussed in the following paragraphs.

3.3.1. Catalyst Coated Membrane

The CCM configuration was developed for the first PEMWEs by General Electric in 1960s,[97] and is the most prominent MEA type nowadays. The CCM is produced by either direct deposition of a catalyst layer on the membrane[21] or by deposition of a catalyst layer onto a medium Teflon substrate, then hot-pressed onto the membrane (decal transfer).[15] A prominent advantage of CCMs is their excellent contact between the catalyst layer and the membrane, resulting in an optimized electrode–membrane interface, so that a low ionic interface resistance is the product. While direct spraying of the catalyst onto the membrane is sometimes applied, this does usually lead to insufficient quality of the resulting MEAs, as the solvent in the catalyst ink typically leads to a swelling and wrinkling of the membrane and thus, the MEA. Therefore, the decal process is applied for manufacturing which consists of deposition of the catalyst layer on a Teflon blank and then hot-pressing the catalyst coated Teflon blank together with the membrane. By adjusting the catalyst layer deposition and the hot-pressing parameters appropriately, high quality MEAs are achieved that can be manufactured in roll-to-roll processes.

Alkaline electrolyzers nowadays still operate at current densities in the range of 0.2–0.6 A cm^{-2}. CCM-type PEMWEs were already reported in 1973 to achieve 1 A cm^{-2} at 1.88 V and 2 A cm^{-2} at 2.24 V and operation duration of 15 000 h with only minor degradation.[98] These early cells were designed to produce the oxygen supply in submarines, thus the cost factor

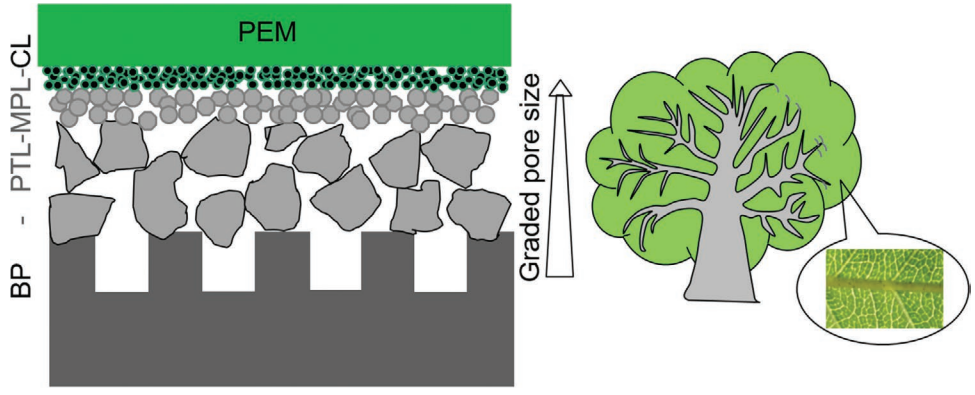

Figure 4. Illustration of hierarchical, graded porous size distribution of the desired electrode structure (left image) mimicking the venation system of a tree (right image).

was only of minor importance. Indeed, the precious metal loadings for both anode and cathode were as high as 1–5 mg cm^{-2}, which is unacceptable for hydrogen production with respect to the targets defined in Fehler! Verweisquelle konnte nicht gefunden werden.[97] In an attempt to develop high performing PEMWEs for the production of H_2 as an energy carrier, Fuji Electric Corporate Research and Development Ltd reported an advancement in PEMWE technology in 1997.[99] In the study, the CCM was formed by decal transfer like described above. With an IrO_2 loading of 4 mg cm^{-2} on the anode and a 51 µm thin membrane, the cell achieved 1 A cm^{-2} at 1.53 V and 3 A cm^{-2} at 1.67 V as well as over 1000 h operation without voltage degradation. While achieving very high cell performance, the study did not aim on low catalyst loadings. Also, the use of such a thin membrane is problematic with respect to H_2 crossover and membrane creeping in practical applications.

The reason for using such high OER catalyst loadings in the early development stage might be due to the lack of ionic conducting and porous network within the catalyst layers due to the use of non-ionic conductive PTFE binder and large Ir particles in the anodes. This leads to a lower utilization of IrO_2 catalyst in the catalyst layers. Also, when cost does not play a central role, the design of a high performance cell is comparably simple. The knowledge of how to achieve optimal catalyst layers in fuel cells could unfortunately not be transferred directly to PEMWEs. This was because the OER catalyst did not have a high surface area support like the analogous carbon supported Pt catalysts for oxygen reduction reaction in fuel cells. Also, the transport phenomena within the anode side are different from that occurring in fuel cells as the oxygen evolving anode is completely wetted, whereas in the fuel cell, a delicate water balance is needed. Also, in the PEMWE anode, voltages above the reversible voltage and acidic conditions result in very harsh conditions which make different supports such as titanium necessary. A question then arises: when a low catalyst loading is used, what is the optimum design of catalyst layers to achieve the required performance? As discussed in Section 3.3, an optimal catalyst layer should have a high ECSA and optimum conditions for the three transport factors. There are two central influence factors for that in typical catalyst layer designs: an optimal ionomer content and a good dispersion of catalysts in highly porous and conductive catalyst layers to optimize the catalyst utilization.

Catalyst Loading: Optimization of catalyst loading is important for maximizing Ir utilization and facilitating mass transport within the catalyst layers.[100] This should be combined with optimizing the catalyst layer manufacturing process to obtain highly porous nanostructured catalyst layers. Conventional catalyst layers have optimal loadings in the range of 1–2 mg cm^{-2}.[15] The low Ir loading often result in low catalyst utilization as mentioned in Section 3.2.2. As discussed in the introduction, the loading of 1–2 cm^{-2} is still considered too high. Recently, Danilovic's group reported substantially improved catalyst layers by simply improving the spray coating process to achieve optimized porous structures of catalyst layers.[101] By optimizing the catalyst ink composition with low solid concentrations of <0.1 wt%, highly mesoporous catalyst layers with Ir loadings from 0.0035–0.17 mg_{Ir} cm^{-2} were fabricated. The resulting catalyst layers were homogeneous even at ultralow loadings of 0.0035 mg_{Ir} cm^{-2}. The authors found that the highest mass activity was obtained for a catalyst layer with loading of 0.011 mg_{Ir} cm^{-2}. This resulted in an Ir–SP of 59 kW g_{Ir}^{-1} at 1.6 V (N117 membrane, 178 µm), which exceeds the critical value for Ir–SP in Table 2 and can be considered a great success. This demonstrated that the intrinsic activity of IrO_x catalysts is sufficient for widespread market application of PEMWEs even with the limited Ir reserves as aforementioned in the introduction. Unfortunately, no stability evaluation was shown in the research. Also, the current density at 1.6 V was only 0.44 A cm^{-2}, which may diminish the deployment of this cell, concerning the levelized CAPEX aspects. Also, for low loading catalyst layers, long term stability is a very big challenge.

Ionomer Content: The ionomer (generally being Nafion) in the anode catalyst layers has two functions: binding the catalyst particles to a uniform layer thus forming the catalyst layer on the one hand and the formation of a proton conducting phase across the porous network of the catalyst layers on the other hand. Without the ionomer, the porosity of a catalyst layer is a result of the inter particle distance of the catalyst powder, which is centrally dependent on the morphology of the catalysts. For example, if excluding the ionomer, commercial catalyst layers composed of $Ir_{0.5}Ru_{0.5}O_2$ catalyst present a porosity of 55% (FuelCellsEtc),[102] whereas, a catalyst layer formed by IrO_2/TiO_2 catalyst has a porosity of 72% (Umicore).[16] The addition of ionomer on the one hand enhances proton conductivity, but on the other hand occupies the porous space, which negatively affects the mass transport and electronic connectivity of the catalyst particles. Therefore, an optimum ionomer content should be aimed for, being a compromise of three factors: proton conductivity, electron conductivity, and mass transport. By an extensive analysis of all voltage losses in the cells, Bernt and Gasteiger found that the optimum ionomer content for a catalyst layer comprising of IrO_2/TiO_2 catalyst (2 mgIr cm^{-2}) is 11.6 wt% as shown in **Figure 5**Aa.[16] This results in a well-balanced porous structure of catalyst layers, which comprises of ≈35 vol% of ionomer, 28 vol% of catalyst, and 37 vol% porosity. This optimum volume composition is in agreement with a modeling analysis using reconstructed 3D microstructure to calculate the tortuosity of the transport parameters.[102]

If the ionomer content is lower than this optimum amount, the ionic resistance (R_{H+an}^{eff}) of the anode increases, thus increasing its associated overpotential ($\Delta E_{H+,an}$) (Figure 5Ba). If the ionomer content is in particular higher than 20 wt%, the ionomer takes up as large part of the pore space, which leads to mass transport limitations and lower electrical conductivity of the catalyst layers (Figure 5Ab,Bc). With the optimum ionomer content, the $\Delta E_{H+,an}$ and η_{mt} losses of the anode become minor with values of 10–20 mV and 10–15 mV at 3 A cm^{-2}, respectively (Figure 5Bb). As the volume fraction of the ionomer is decisive for the transport processes, the optimum ionomer content is dependent on the morphology of the catalyst (catalyst density) and the wetting behavior between the catalyst and the ionomer, and thus specific for each catalyst material. Unsupported IrO_x particles catalysts which have higher density have lower optimum ionomer contents than supported catalysts. It has been found that catalyst layers with IrO_2 (99.9%, Alfa Aesar) have an optimal ionomer content of 5 wt%.[103]

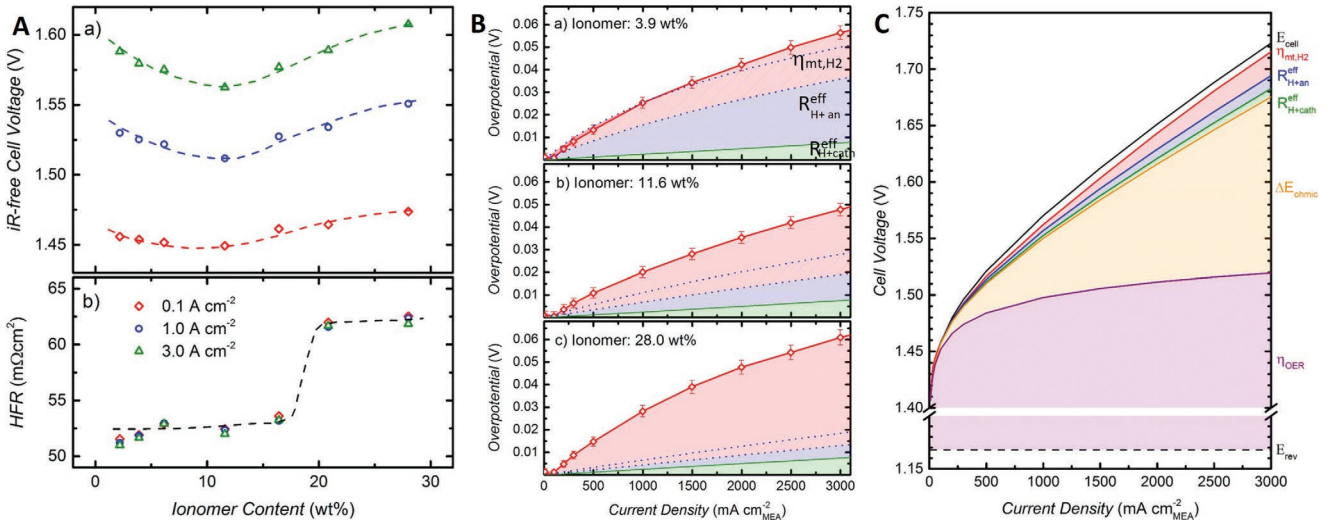

Figure 5. Dependence of ionomer contents of the anode on cell voltage losses. A) iR-free cell voltages (a) and HFR (b) of the cells at different current densities as a function of ionomer content. B) Overpotential breakdown after subtraction of ohmic and kinetic losses for the different ionomer contents. C) Cell voltage breakdown to different loss components: E_{cell}–overall cell voltage, $\eta_{mt,H2}$–mass transport loss, R^{eff}_{H+an} –anode–ionic resistance loss, R^{eff}_{H+cath} – cathode–ionic resistance loss, ΔE_{ohmic}–ohmic loss, η_{OER}–OER overpotential loss, E_{rev}–reversible cell voltage. Adapted with permission under the terms of the Creative Commons CC BY license.[16] Copyright 2016, the Authors. Published by ECS.

This catalyst layer delivered high cell activities of 1 A cm^{-2} at 1.54 V and ≈1.6 A cm^{-2} at 1.6 V at Ir loading of 0.36 mg cm^{-2}, corresponding to an Ir–SP of 6.6 kW g_{Ir}^{-1} at 1.6 V with N212 membrane (thickness of 50 µm). However, this is still a factor of 7 lower than the critical Ir–SP in Table 2. Further reducing Ir-loading to lower than 0.36 mg cm^{-2} unfortunately resulted in lower cell performance due to too low activity per geometric cell area.[103] For conventional IrO_2 catalysts, when the Ir-loadings are lower than ≈0.4 mg cm^{-2}, the catalyst layers become too thin and inhomogeneous. Cracks can be present in the catalyst layers, making the in-plane electric conductivity insufficient, and result into low catalyst utilizations.[15,78] Therefore, further strategies for highly efficient catalyst layers such as using advanced catalysts or catalyst supports are needed.

Supported Catalysts for Efficient Catalyst Layers: Catalyst layers using conventional unsupported IrO_2 catalysts have thicknesses scaling with Ir-loadings at a factor of ≈3 µm $(mg_{Ir}\ cm^{-2})^{-1}$ (denoted as thickness factor).[78] A loading of <0.4 mg cm^{-2} will result in catalyst layer thicknesses lower than 1.2 µm, which causes not only issues in the catalyst layer integrity, but also in mass transport limitations.[101] At low loadings, not only the electrical conductivity, but also proton transport and O_2 removal are limited. This is due to the reduced interfaces between the PTL and catalyst layer, so that the triple phase contact area is lower. All protons and O_2 are produced at these reduced areas, leading to transport limitations. Catalyst supports help to increase the catalyst dispersion and electrical conductivity within the catalyst layer, and in turn, its utilization. As demonstrated in fuel cells, the use of carbon-supported Pt leads to a reduction of an order of magnitude in Pt loading. Due to the corrosive conditions within the anode of PEMWE (potential >1.4 V and low pH), selections of OER catalyst supports are restricted to limited candidates that are stable enough under OER working conditions. For example, Rozain et al.[80] published one of the first systematic studies to use Ti microparticles with diameters (1.24–40 µm) as a catalyst support to form IrO_2/Ti mixture with wt. ratio 1:1. As a result, the thickness factor increased to ≈5.8 µm $(mg_{Ir}\ cm^{-2})^{-1}$ (**Figure 6**A). The electrical conductivity (measured as high frequency resistance, HFR) and performance of the catalyst layers allowed loadings below 0.4 mg cm^{-2} of IrO_2. These were in contrast to those of the unsupported IrO_2 particles, which showed degrading performance at IrO_2-loadings below 0.4 mg cm^{-2}, as shown in Figure 6B,C. The cell performance with 0.12 mg_{IrO2} cm^{-2} (0.1 mgIr cm^{-2}) of IrO_2/Ti catalyst was comparable to the cell with 0.32 mg_{IrO2} cm^{-2} (0.27 mgIr cm^{-2}) of pure IrO_2, but IrO_2/Ti catalyst showed much better durability after 1000 h operation (Figure 6C). This performance resulted in an Ir–SP of 7.4 kW g_{Ir}^{-1} at 1.6 V with a N115 membrane (127 µm thick).

Due to the highly oxidative operating conditions at the anodes, the Ti-micropaticle supports are anticipated to be eventually oxidized to TiO_2 during long term operation. Commercial catalysts use TiO_2 supports instead of metallic Ti, wherein the IrO_2 is mixed with TiO_2 nano-/microparticles during synthesis to form a IrO_2/TiO_2 composite. IrO_2@TiO_2 core-shell microparticles were shown to be more promising in terms of catalyst utilization.[66] TiO_2 supports are not a good electric conductor. An important property of the IrO_2 and RuO_2 oxides is that they have high electron conductivity despite being oxides.[104] Consequently, the catalyst must be covered on the support, so that it is percolating on the catalyst support. Therefore, the IrO_2 content normally accounts for >40 wt % to ensure electron percolation pathway for the composite catalysts.[104–106] Bernt et al. extensively optimized and analyzed the performance of the catalyst layers of this catalyst at different Ir-loadings between 0.2 and 5.41 $mg_{Ir}\ cm^{-2}$.[15] The obtained catalyst layers have a thickness factor of ≈4 µm $(mg_{Ir}\ cm^{-2})^{-1}$. This supported catalyst achieved an Ir–SP of 12.5 kW g_{Ir}^{-1} at 1.79 V (80% HHV efficiency), but a low Ir–SP of 1.85 kW g_{Ir}^{-1} at 1.6 V at loading of 0.2 $mg_{Ir}\ cm^{-2}$. This inefficiency of a low Ir-loading catalyst layer was explained

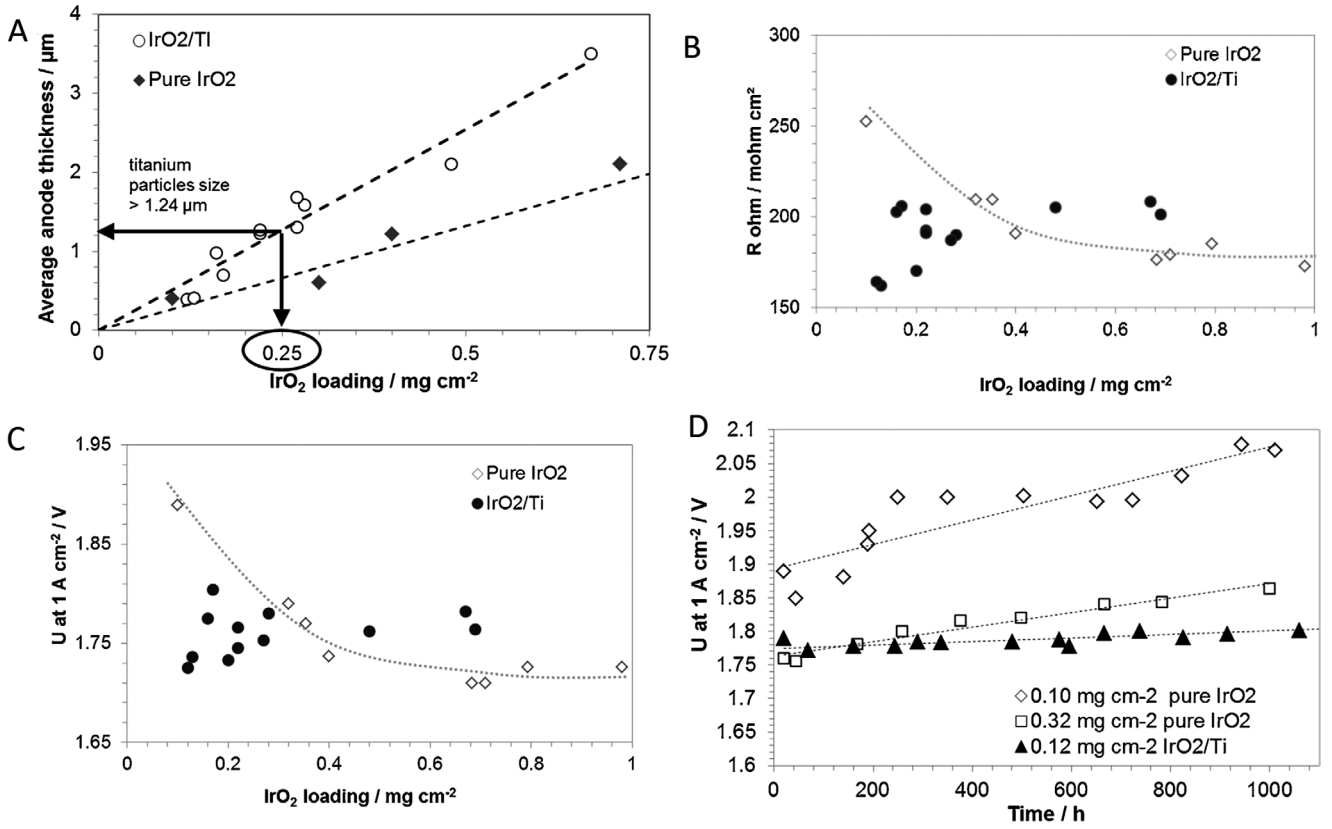

Figure 6. Comparative performance of Ti-microparticle supported and unsupported IrO_2 catalysts with different loadings. A) Average thickness of anode as a function of loading. B) Ohmic resistance of the cells as a function of catalyst loadings. C) Cell voltage at 1 A cm^{-2} as a function of catalyst loading. D) Cell durability tests by holding current at 1 A cm^{-2}. Reproduced with permission.[80] Copyright 2016, Elsevier.

by the inhomogeneous integrity of the catalyst layer, which contained some isolated catalyst islands not being used. As a result, a low catalyst utilization was observed. This also resulted in a larger Tafel slope of 68 mV dec^{-1} for the low loading cell (0.2 mg_{Ir} cm^{-2}) compared to that of 47 mV dec^{-1} for the higher loading cell (1.58 mg_{Ir} cm^{-2}). The bad performance could also be caused by the low electrical conductivity of TiO_2 support, leading to inefficient in-plane electron conductivity of the thin catalyst layer, evidenced by the high HFR for the low Ir-loading cell. The electrical conductivity of the support is an important metric toward low Ir-loading catalyst layers. Doping TiO_2 with a foreign element such as Nb,[107,108] V,[109] and W[110] can increase its electrical conductivity. Zhao et al.[110] reported a promising performance of 38 wt% Ir nanoparticles loaded on $W_xTi_{1-x}O_2$ catalyst. The IrO_x nanoparticles are well-dispersed on the support particle, making its morphology similar to a typical Pt/C catalyst as shown in **Figure 7**A,B. With this good dispersion, the resulting catalyst layer with 0.4 mg_{Ir} cm^{-2} has a significantly improved thickness factor of 37.5 µm $(mg_{Ir}\ cm^{-2})^{-1}$, and Ir-SP of ≈3 kW g_{Ir}^{-1} at 1.6 V (N115 membrane, 127 µm). The thickness factor with this manufacturing approach was one order of magnitude higher than comparable catalyst materials using conventional coating process.[78,103] The cell demonstrated a degradation rate of 16.7 µV h^{-1} in a stability test consisting in holding current at 1.5 A cm^{-2} for 1200 h (Figure 7C,D). Doped SnO_2 is also a promising candidate to be used as support for Ir catalysts, as it presents high conductivity and a decent stability in the OER conditions. Ohno et al.[111] investigated OER catalysts, which are based IrO_x nanoparticles loaded on M-doped SnO_2 (M is Nb, Ta, and Sb). The authors found that Sb-SnO_2 (ATO) is the best support candidate among the M-doped SnO_2. This resulted in the high conductivity of Sb-SnO_2 supported IrO_x catalyst. Consequently, the cell delivered an Ir–SP of 10.8 kW g_{Ir}^{-1} at 1.6 V (NRE212 membrane, 50 µm). However, a previous study showed insufficient stability of ATO under OER working conditions due to the dissolution of Sb and Sn.[112,113]

Nanostructured Catalyst Layers: Apart from using supported catalyst to achieve high dispersion, there are also methods available to directly create nanostructures of unsupported catalysts and catalyst layers which are discussed below.

Catalyst layers can be fabricated directly during synthesis of IrO_x nanoparticles by a flame-based reactive spray deposition technology (RSDT). This method enables embedding IrO_x nanoparticles into Nafion ionomer, thus forming a catalyst layer with high porosity (thickness factor of 25–31 µm mg_{Ir}^{-1}) and good transport network connection for all three transport phases. Therefore, it was used to fabricate low Ir-loading anodes.[85,114] It was found that a loading of 0.08 mg_{Ir} cm^{-2} was an optimal value for anodes fabricated by this method[38] The resulted cell exhibited 1.875 V at 1.8 A cm^{-2} using a 178 µm thick membrane (N117). This corresponds to an Ir–SP of 33.3 kW g_{Ir}^{-1} at energy efficiency of 76.4%. The cell demonstrated 4500 h operation with degradation rate of 36.5 µV h^{-1} during first 2500 h and 11.5 μV^{-1} for the period of 3500–4500 h.

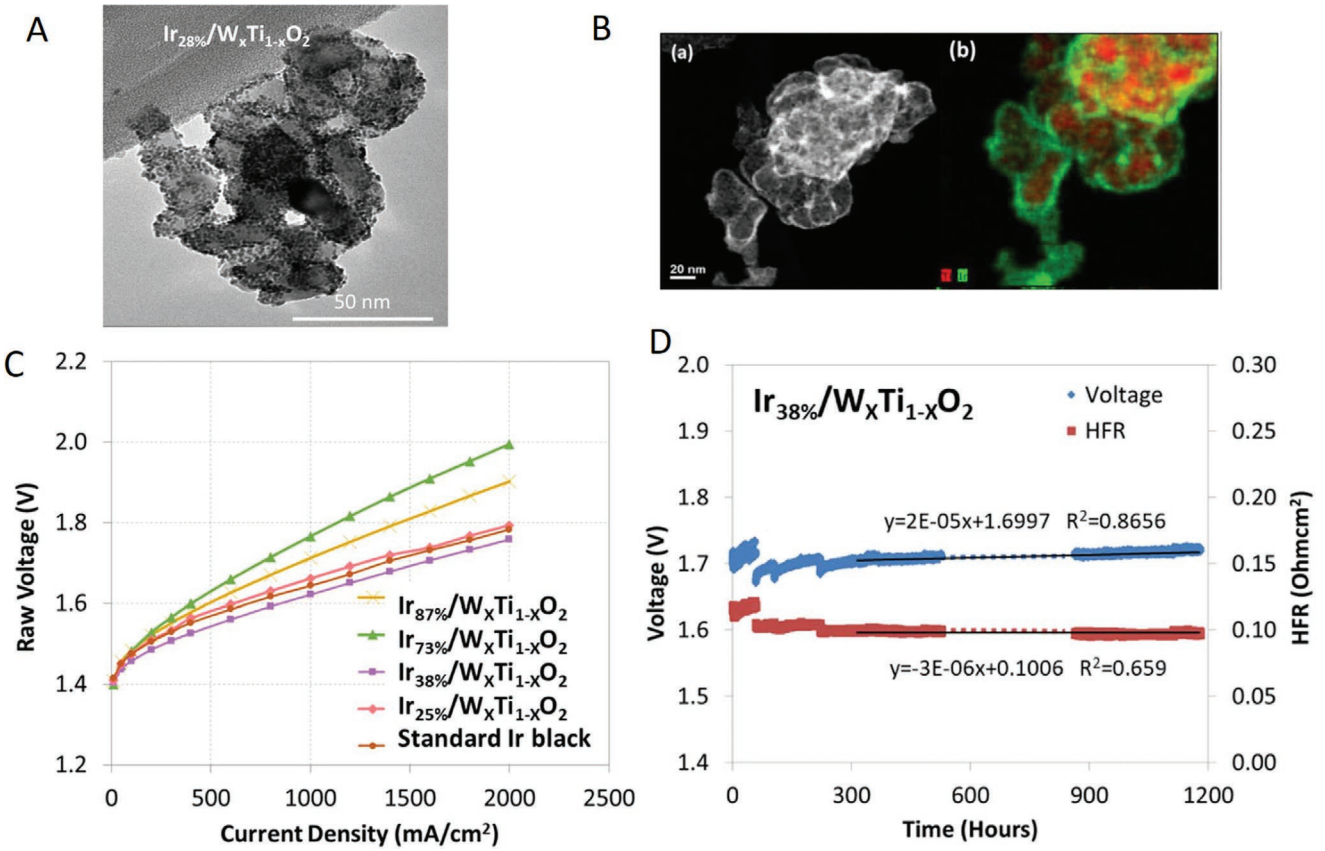

Figure 7. A) Transmission electron microscope image and B) Energy-dispersive X-ray spectroscopy (EDX) elemental map of 38 wt% Ir nanoparticles loaded on $W_xTi_{1-x}O_2$ catalyst. C) Polarization curves of the cells using the supported Ir catalysts with different Ir contents. D) Cell durability tests by holding current at 1.5 A cm^{-2}. Reproduced with permission.[110] Copyright 2018, IOP Publishing.

This was a remarkable performance, given the low loading and thick membrane used.

Another approach is the nanostructured thin film (NSTF) catalysts such as, for example, developed by 3M which are catalyst of unique structure with high activity as shown in **Figure 8**A.[115] The 3M NSTF catalyst has a core-shell structure with a core nanowire or whisker out of crystalline organic materials and a thin shell of precious metals (Figure 8A). The whisker cores out of perylene are single crystals, having highly uniform surface for a subsequent coating with catalytic materials such as Pt or Ir. The thin films of precious metals are produced by vacuum physical deposition that enables a large specific surface area of the precious metals to be used for catalysis. The perylene core is a p-type organic semiconductor that has high resistance to corrosion at >2 V. With 0.25 mg_{Ir} cm^{-2} loading, anodic catalyst layers using NSTF catalyst showed an Ir–SP of ≈6 kW g_{Ir}^{-1} at 1.6 V, and almost no degradation during durability tests that were performed by holding a current at 2 A cm^{-2} for 5000h (Figure 8B,C).[115–117] Nevertheless, the Ir–SP value was still significantly lower than the target value given in Table 2.

The strategies previously discussed are mainly aiming at enhancing the number of active sites of the catalyst layers. Although substantial improvements have been achieved, further improvement in intrinsic activity of the catalysts might be a viable solution to achieving both critical values of Ir–SP and cell activity.

Intrinsically Enhanced Activity Catalysts: Instead of increasing the surface area per unit area of a given catalyst, which is a structural approach, another approach is to increase the activity per active site on the catalyst. The intrinsic activity of a catalyst manifests in the rate of OER at an active site, typically expressed as turnover frequency (TOF). If the intrinsic activity of the catalyst could be increased, lower loadings could be achieved. Promising approaches for this include alloying IrO_x catalysts with other metals such as Ru or Ni. RuO_2 as an OER catalyst is often found more active than IrO_x in half-cell characterizations.[83] However, in both PEMWE and half-cell operation RuO_2 is quickly deactivated and/or dissolved, thus leading to significantly lower cell performance than IrO_2 after short operation times.[99,118] When alloying Ir with Ru to form $Ir_xRu_{1-x}O_2$, on the one hand, the Ru elements can enhance the intrinsic activity of the bimetallic mixed oxide catalysts, on the other hand, Ir can stabilize the Ru elements within the alloys. Aricò et al. extensively developed the implementation of $Ir_xRu_{1-x}O_2$ catalyst in PEMWE in a series of studies.[32,81,82,119] The catalysts were synthesized using a modified Adam's fusion method. The stoichiometric ratio of IrO_2 and RuO_2 is 70:30, ensuring the complete solubilization of RuO_2 into the IrO_2 lattice to form homogeneous $Ir_{0.7}Ru_{0.3}O_2$. An acid leaching step was applied to remove Ru on the surface to obtain Ir-surface rich catalyst particles for enhanced stability. Notably enhanced performance was observed for the cell using $Ir_{0.7}Ru_{0.3}O_2$ compared to

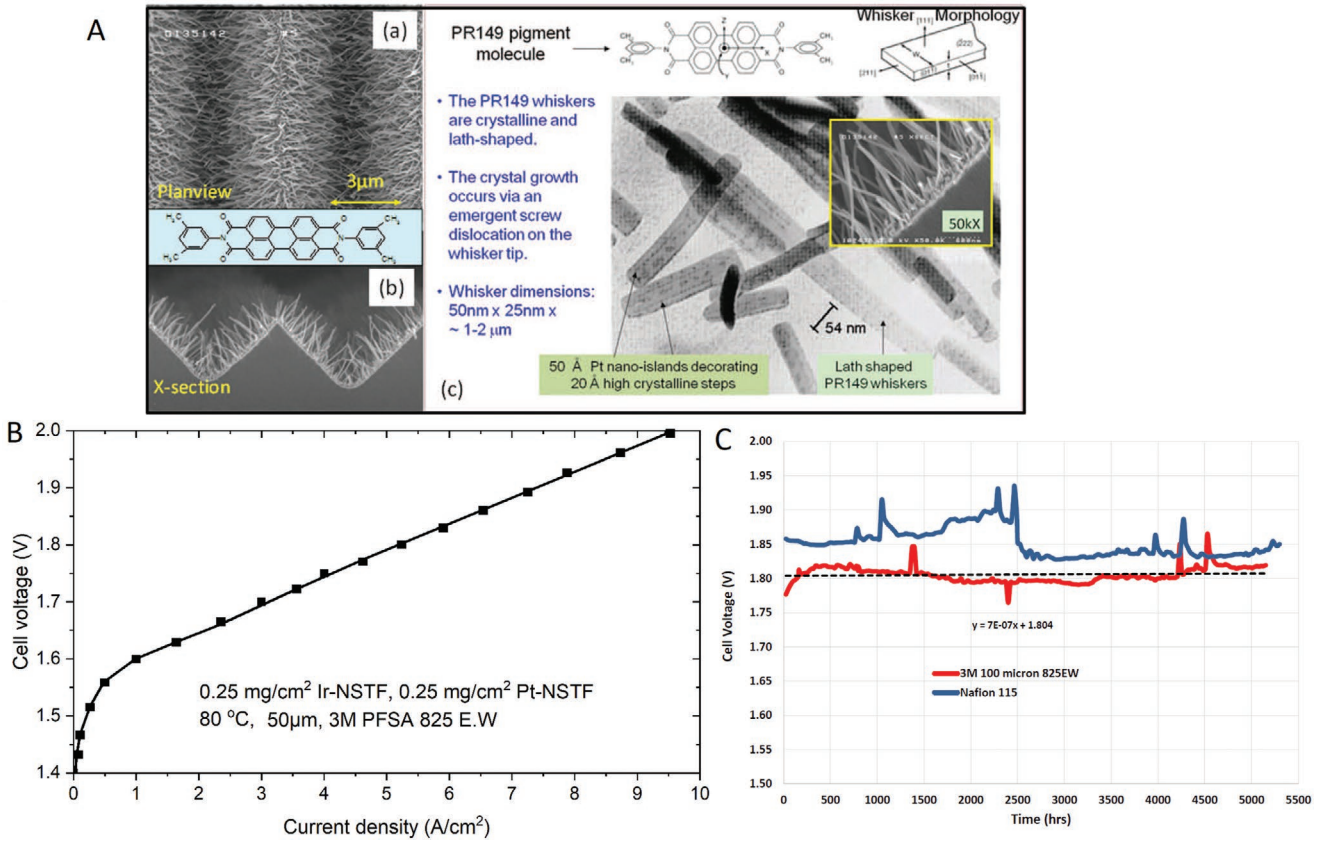

Figure 8. A) Morphology of the nanostructured thin film (NSTF) catalyst developed by 3M company. B,C) Polarization curves and stability tests by constant current holds of the cells using NSTF catalyst with different membrane thicknesses. Reproduced with permission.[115–117] Copyright 2012, ECS.

pure IrO_2 catalyst (**Figure 9**A). The catalyst layers of this catalyst have a thickness factor of ≈10 μm $(mg_{IrRu}\ cm^{-2})^{-1}$, which is significantly higher than that of ≈3 μm mg_{Ir}^{-1} for conventional IrO_2.[78] An online dissolution analysis using a flow cell connected with inductively coupled plasma mass spectrometry (ICP-MS) showed that the dissolution rate of metal elements occurred mainly at high potential (e.g., ≥1.8 V vs RHE). The dissolution rate scaled with the metal concentration at the surface of the catalyst as shown in Figure 9B.[82] With a Ir-rich surface, Ru dissolution from $Ir_{0.7}Ru_{0.3}O_2$ was significantly smaller than Ir. Figure 9B,C shows the polarization curves and durability test data of catalyst layers with 0.3 $mg_{IrRu}\ cm^{-2}$ loading.[120] A cell with a 50 μm thin membrane achieved 1.3 A cm^{-2} at 1.6 V, corresponding to an Ir–SP of 9.2 kW g_{Ir}^{-1} or an IrRu–SP of 6.4 kW g_{IrRu}^{-1} if taking Ru into account. The cell showed a degradation rate of 20 μV h^{-1} during the hold of a relatively high current at 4 A cm^{-2} for 3500 h. As can be seen in Figure 9D, the cell voltage was almost constant during the last 2500 h test period. A PtCo-recombination catalyst was also added to the anode to eliminate the H_2 crossover for coping with the safety issue when using 50μ thin membrane. Its incorporation decreased the cell activity to a small extent, but showed improved activity during long-term operation as shown in Figure 9C,D.

Amongst transition metals, Ni has been proven to be the most promising one for alloying with Ir to enhance its OER specific activity.[121,122] Similar to Ru, in order to improve the stability, an acid-leaching step is applied to remove surface Ni to create an Ir-rich surface of the alloy catalyst particles. It is discussed that the leached Ni creates lattice vacancies within the surface of the catalyst particles, which could be an additional structural effect. This might create the so-called d-band holes in iridium elements and holes on oxygen ligands adjacent to the lattice vacancies. Those holes are argued to enhance the intrinsic activity of the catalyst toward the OER.[29,122] Alia et al.[123] synthesized Ir–Ni nanowires by galvanic displacement deposition on a Ni nanowire precursor. This catalyst has a benefit in both intrinsic activity and high specific electrochemical surface area. As a result, its catalyst layer exhibited a good performance of 1 A cm^{-2} at 1.6 V at loading as low as 0.1 $mg_{Ir}\ cm^{-2}$, corresponding to Ir–SP of 14.8 kW g_{Ir}^{-1}. In this work, no durability data for the PEMWE cell were shown.

Considering both durability and activity, the alloyed $Ir_{0.7}Ru_{0.3}O_2$[120] is very promising with Ir–SP of 9.2 kW g_{Ir}^{-1} and cell activity of 1.3 A cm^{-2} at 1.6 V, respectively. Though, this Ir–SP is still a factor of five below the critical value. As previously discussed, even with an optimal catalyst layer, the Ohmic resistance overpotential accounts for a large portion of the overall voltage loss. This ohmic resistance is measured as HFR of the cell, which consists of ionic conduction resistance of the membrane (R_{mem}), electronic setup (R_e), and interfacial resistance (R_{inter}) between the catalyst layer and

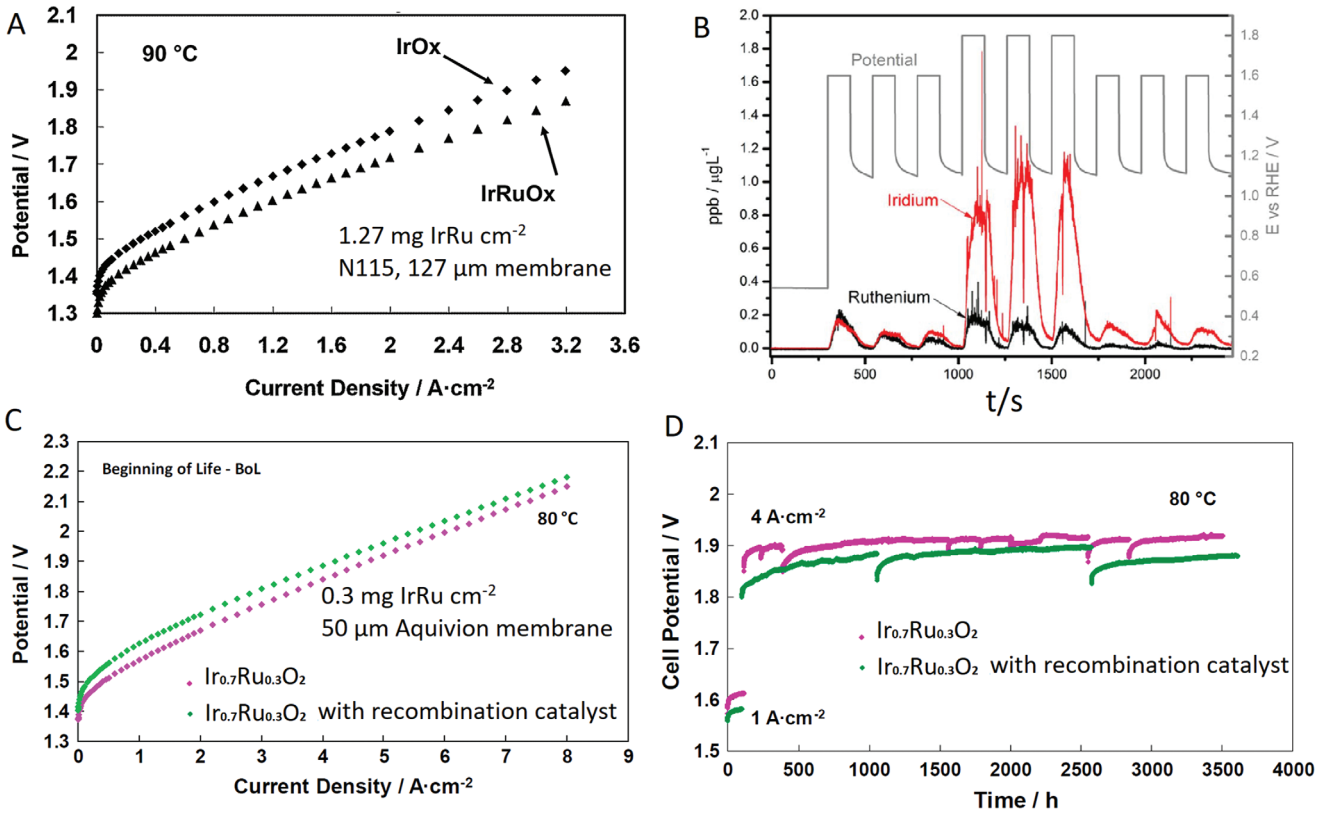

Figure 9. A) Performance of cell using $Ir_{0.7}Ru_{0.3}O_2$ compared to IrO_2 catalyst. Reproduced with permission.[32] Copyright 2015, Elsevier. B) An online catalyst dissolution analysis using flow cell connected with inductively coupled plasma mass spectrometry (ICP-MS). Reproduced with permission.[82] Copyright 2017, Elsevier. C,D) Performance and durability of the cells using $Ir_{0.7}Ru_{0.3}O_2$ catalyst with a 50 µm thin membrane with and without recombination catalyst. Reproduced with permission.[120] Copyright 2020, Elsevier.

PTL: HFR = R_{mem} + R_e + R_{inter}. While R_{mem} is the dominant component of conventional catalyst layers, R_{inter} can have a significant contribution if low Ir-loading catalyst layers are used.[15,80]

Research and development on alternative OER catalysts to Ir and Ru based counterparts are challenging, although some progress has been made. For example, manganese oxide (MnO_x), gamma manganese oxide (g-MnO_2), or $CoFePbO_x$ have been tested as OER catalysts in both half-cell and full cell PEMWE.[124–126] However, both activity and stability were significantly lower than Ir and Ru based catalysts. Substantial improvement needs to be accomplished in future research before this class of non-noble metals based OER catalyst becomes viable for practical applications. From our standpoint, Ir and Ru based catalysts are still indispensable for practical applications in the near future. Alternatively, some new molecular structures of Ir and Ru have been developed such as $IrO_x/SrIrO_3$,[127] Ru-based pyrochlores,[68] Ru-based perovskite oxides,[128] or Cr doped Ru-oxide.[129] These materials showed enhanced intrinsic activity that is very exciting and promising for further reduction in noble metal loadings in PEMWE applications, if their stability is appropriately enhanced.

In the next section, we will discuss approaches aiming to improve the interfacial resistance between catalyst layer and transport layers which actually results into important design criteria for catalyst layers.

3.3.2. Porous Transport Electrode

PTL/CL Interface: Several studies have found that the HFR of the cell increases significantly when low loading anodes are used, while keeping the same membrane and basic cell setup.[15,80] For example, Bernt et al.[15] observed an HFR increase by 30–40% for 0.2 mg_{Ir} cm^{-2} compared to 1.58 mg_{Ir} cm^{-2} loading catalyst layer (**Figure 10**A). This increased resistance could be attributed to an increase of R_{inter} when thin catalyst layers were used as the result of low catalyst loading. The electron transfer from catalyst active sites to the PTL occurs at these interfaces, namely at the contact area between the Ti fibers and the catalyst layer. But before reaching the interfaces, the electrons must travel through-plane and/or in-plane direction within the catalyst layer, experiencing electrical resistances within the catalyst layer. While the through-plane resistance is low due to short distances, the in-plane resistance is relatively high due to the long length scale (10–50 µm) between Ti-fibers of the PTL. Moreover, the thin catalyst layers are often inhomogeneous, containing cracks or event isolated catalyst parts due to the stress and strain caused by the compression (Figure 10B). This exacerbates the in-plane resistance, and interfacial resistance as a result, and also results in lower catalyst utilization. In a study on the influence of different PTL properties on PEMWE performance, Schuler et al.[22] found that the anodic catalyst utilization increased with the interfacial area. Surprisingly, Zhang

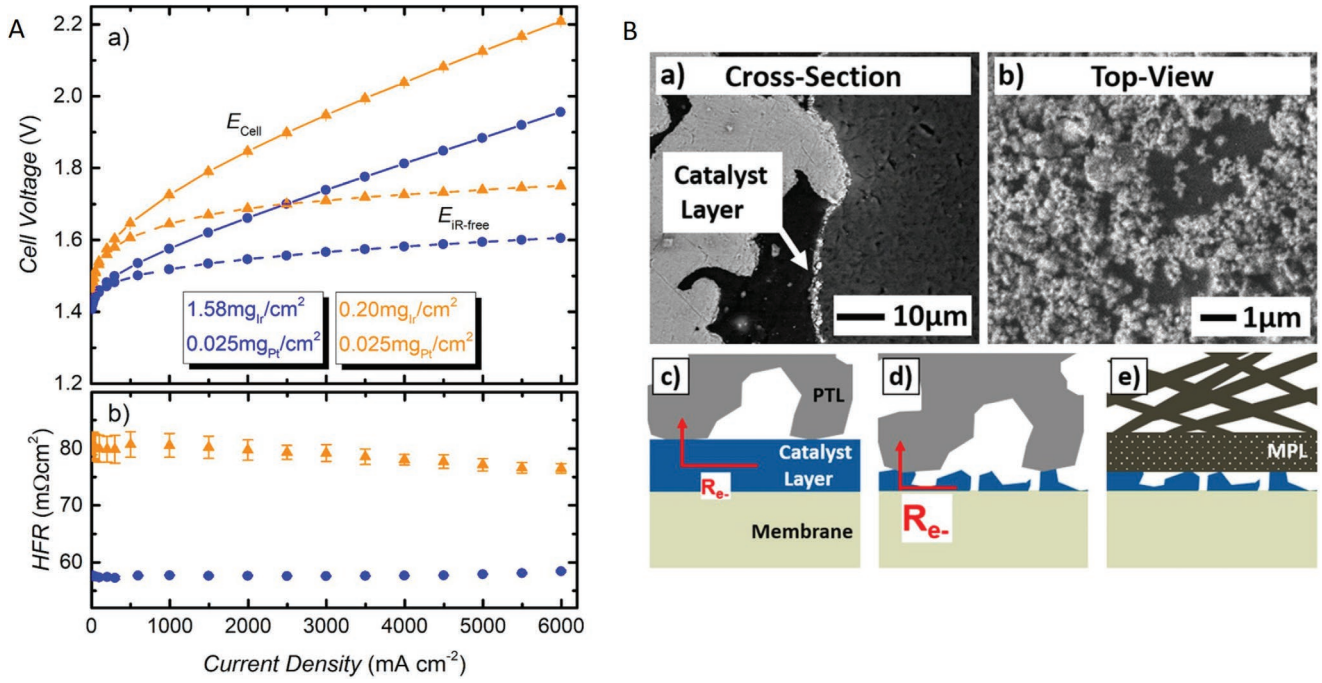

Figure 10. A) Performing comparison of the cells using low catalyst loading (0.2 mg_{Ir} cm^{-2}) and conventional loading (1.58 mg_{Ir} cm^{-2}). B-a,b) Cross-section and top-view of scanning electron microscope (SEM) images of the anode with the low catalyst loading, c,d) schematic illustration on the cause of resistance for high and low loading anodic catalyst layers, and e) the model catalyst layer with MPL. Reproduced with permission under the terms of the Creative Commons CC BY license.[15] Copyright 2018, the Authors. Published by ECS.

et al. discovered that the OER only occurred at the parts of catalyst layer adjacent to the current collector of the PTLs.[130] As a model to demonstrate the importance of the interface, Bernt et al.[15] used a carbon gas diffusion layer (GDL) with a microporous layer (MPL) in place of the Ti-PTL (Figure 10B,e). As a result, the catalyst utilization of the low loading catalyst layer with 0.2 mg_{Ir} cm^{-2} became comparable with the one with 1.58 mg_{Ir} cm^{-2} loading. Moreover, surface Ti on the PTL is known to be oxidized during long term operation, increasing the interfacial resistance.[131] Therefore, improvement of the interface properties toward lower resistances is necessary for the development of low loading anodic catalyst layers. Besides using Pt or Au coated PTLs which adds cost, alternative strategies might be the development of a Ti-porous backing layer (PBL) on the PTL, and a direct coating of Ir-based catalysts onto the Ti-PTL or Ti-PBL/PTL to form a so-called catalyst coated porous transport electrode (PTE).

Catalyst Coated PTL: Unfortunately, the fabrication of Ti-PBLs with high porosity and pore size equivalent to the carbon based MPL layer of fuel cells is extremely difficult, and has not been reported in literature so far. As an intermediate step, Thiele et al.[100,132,133] developed in a series of studies, direct coating catalyst onto PTLs to form PTEs. The results of cell activity were at least comparable with conventional CCM based cells. In addition, the cells showed good durability in a preliminary test in a current hold at 2 A cm^{-2} for 200 h.[100] The same research group later designed a novel catalyst which aimed to be structurally compatible with the large pores within the large, micrometer sizes pores of the PTLs to improve this PTE configuration.[66] The catalyst developed was based on IrO_2 coated TiO_2 core-shell microparticles. The large diameters of the catalyst particles were supposed to help to avoid the deep penetration of the catalyst particles into PTL during depositing the catalyst layers within the porous transport layers to form electrodes. As a result, better catalyst utilization was achieved with the cell activity being significantly improved, compared to a conventional catalyst and CCM based cell.

With these PTEs, when the catalyst loading decreased from 1.2 mg_{Ir} cm^{-2} to 0.4 mg mg_{Ir} cm^{-2}, the HFR of the cell remained almost constant, demonstrating an improved interfacial contact of this MEA configuration. Another, similar approach showed promising results of IrO_2 supported on ATO.[134] Other than spray coating, the PTEs could be produced by electrochemically depositing Ir directly on PTLs.[135–137] Lim et al.[138] fabricated a PTE by using a sequential electrochemical deposition of Pt particles and IrO_2 shell coated on the Pt particles on Ti-felt, and used it in unitized regenerative fuel cells. The deposited Pt particles with a size of 0.5–1.5 μm acted as a support for the deposition of IrO_2 films with thicknesses of 70 nm, which was an OER catalyst when the cell was operated in PEMWE mode. With an Ir-loading 0.16 mg cm^{-2}, the cell (N212 membrane, 50 μm) exhibited an activity of 1.2 A cm^{-2} at 1.6 V, and a stable, low HFR of 50 mΩ cm^2 during a 300 h stability test. The cell activity resulted in an Ir-SP of 11.1 kW g_{Ir}^{-1} at 1.6 V. The results indicate that this approach is very promising for the fabrication of PTEs with low Ir-loading and low interfacial resistance.

Porous Backing Layer: The aforementioned direct deposition of catalysts on the Ti-PTL has however the drawback that the catalyst is often deposited deeply into the PTL substrate due to the large pore size of the PTL. The deeply deposited catalyst might not be ionically connected to the membrane, and thus not be utilized. Moreover, the coarse surface of Ti-PTLs is a

factor limiting the use of thin membranes, which can result in high local pressures on the membrane causing plastic deformation of the membrane and possibly causing cracks and holes in it. Indeed, it was observed that PTLs with smaller pore sizes but higher porosity showed better cell activity.[139] Therefore, it would be beneficial to implement a PBL providing a smoother interface between Ti-PTL and catalyst layer. This approach could also address the aforementioned issue of insufficient in-plane electric conduction in low-loading catalyst layers. While PBLs composed of carbon particles are widely used in standard fuel cell MEAs, an appropriate PBL for the anode of a PEMWE has not yet been established for commercial systems. One challenge is the harsh working conditions of the anode which do not allow materials made of unstable materials such as carbon. It is logical to foresee that a PBL composed of Ti-micropaticles could be deposited on Ti-PTLs by a conventional coating technique such as spray coating or doctor blading. But this coating process usually requires the use of a binder such as Nafion to form a layer, which can decrease the electrical conductivity of the PBL.[140] In addition, the Ti-microparticles are prone to be oxidized under working conditions, therefore degrading the electrical conductivity of the PBL degrades. Lettenmeier et al.[141] introduced the use of vacuum plasma spraying method to fabricate Ti-gas diffusion layers (GDL) with through-plane gradient pore-size distribution. The pore sizes were customized ranging from ≈5 µm for electrode-facing side to ≈10 µm for bipolar plate-facing side. The gradient in pore-size distribution was proven to reduce the capillary pressure and tortuosity that facilitated the mass transport within the anode. As reported in a recent study by Büchi et al.,[142] PBLs (term MPL used in the original paper) with different surface roughnesses and porosities were produced by sintering layers of Ti microparticles with different diameters as shown in **Figure 11**. The implementation of a PBL on a conventional PTL improved the catalyst utilization by a factor between 2.2–2.8 and reduced the mass transport overpotential by 60 mV at 2 A cm^{-2}, compared to a cell without PBL. These improved performances were explained by a homogeneous distribution of the compression between the catalyst layer and the membrane and higher interfacial contact area between the catalyst layer and the PBL. This all improved the in-plane electrical conduction of the catalyst layer, and thus catalyst utilization.

Despite the promising results of using PBLs, low catalyst loadings for this electrode configuration have not been reported. This could be a viable approach for future development of low loading PEMWEs.

We note that besides electrode structures, the assembly conditions of an MEA such as cell compression and choice of suitable gaskets are also factors which largely influence the HFR of cells, and consequently its performance. The clamping control system and gaskets need to precisely and evenly maintain the clamping pressure over the active area of the MEA to obtain low cell HFR. There is an optimal clamping pressure for each system, which needs to be investigated experimentally to optimize the system performance.[143]

We summarize the most promising cell developments in **Table 4** and compare them with the critical parameters which are required for large scale application of PEMWEs. So far, no

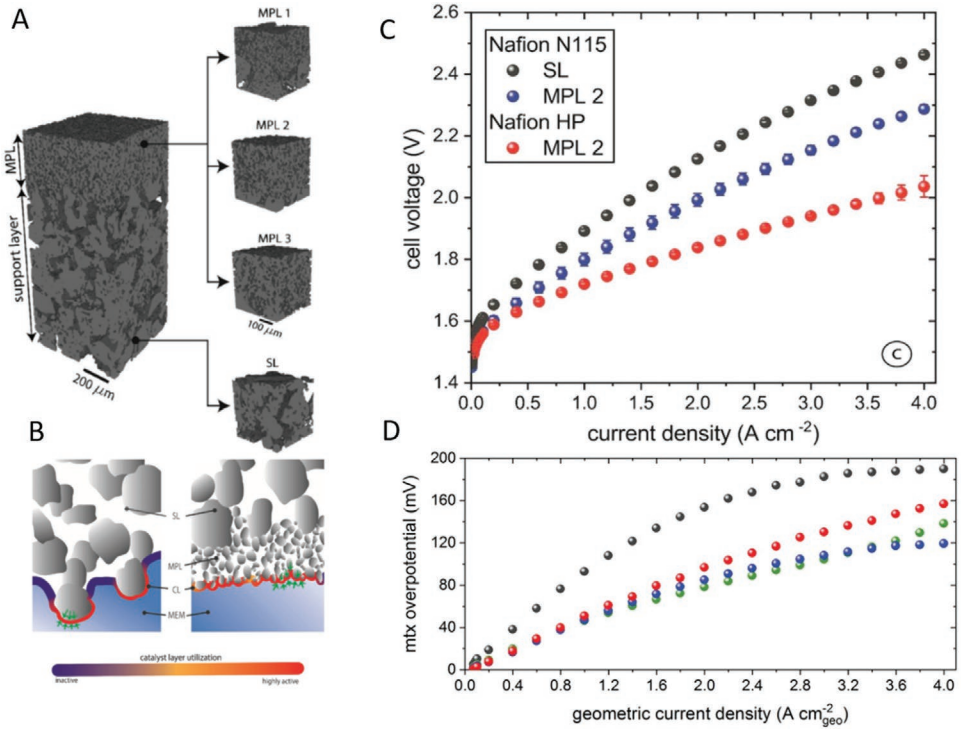

Figure 11. A) Reconstruction 3D images of the anodic electrode with MPLs (PBLs) of different porosity. B) Schematic illustration of the interfaces of the catalyst layer and the GDL or MPLs (PBLs). C) Polarization curves and D) mass transport overpotentials of the electrodes with and without MPLs (PBLs). Reproduced with permission.[142] Copyright 2019, Wiley-VCH.

Table 4. State-of-the-art PEMWEs and evaluation with respect to the critical parameters ("+" and "–" stand for meeting or not meeting the critical parameters, data were calculated based on originally published data).

Catalysts	Ir-loadings [mg_{Ir} cm^{-2}]	PEM thickness [μm]	Cell activity at 1.6 V [A cm^{-2}]		Ir–PD at 1.6 V [kW g_{Ir}^{-1}]		Degradation rate [μV h^{-1}] [Test duration, h]	References
			≥1.0	Evaluation	≥50	Evaluation	≤6	Critical parameters
Early reported IrO_2	4.00	51	2.0	+	0.7	–	Negligible (4000 h)	[99]
IrO_2/TiO_2	0.20	51	0.25	–	1.9	–	NA	[15]
$Ir_{38\%}/W_xTi_{1-x}O_2$	0.40	125	0.8	–	3.0	–	16.7 [1000 h]	[110]
IrO_2	0.36	51	1.6	+	6.6	–	NA	[103]
IrO_2/Ti	0.10	127	0.5	–	7.4	–	Negligible (1000 h)	[80]
RSDT IrO_2	0.08	178	1.8 (1.875 V)[a)]	+	33.3	–	36 (2500 h)	[38]
NSTF IrO_2	0.25	50	1.0	+	5.9	–	negligible (5000 h)	[115]
IrO_2 highly porous CL	0.17	178	0.75	–	6.5	–	NA	[101]
$Ir_{0.7}Ru_{0.3}O_2$	0.30 (Ir + Ru)	50	1.3	+	6.4	–	20 (3500 h)	[120]
$Ir_{0.7}Ru_{0.3}O_2$	0.21(Ir)	50	1.3	+	9.2	–	20 (3500 h)	[120]
IrO_2/ATO	0.11	50	0.8	–	10.8	–	NA	[111]
IrO_2/IrO_2 NW	0.20	50	1.5	+	11.1	–	NA	[21]
IrO_2 PTE	0.16	51	1.2	+	11.1	–	Negligible (200 h)	[138]
Ir–Ni NW	0.10	NA	1.0	+	14.8	–	NA	[123]
IrO_2 3D-printed	0.045	51	0.5	–	16.5	–	NA	[145]
IrO_2 highly porous CL	0.011	178	0.44	–	59.2	+	NA	[101]

[a)]activity at cell voltage of 1.875 V; NA: not available.

reports with cell performance meet all the set critical parameters. To fulfill the criteria for large scale application (Ir–PD), the loadings should be largely constrained; the only report which fulfilled them (ref. [101]) required Ir loading as low as 0.011 mgIr cm^{-2}. This in turn leads to a low current density of 0.44 A cm^{-2} at 1.6 V. The CAPEX cost for this case could be a factor of 3 higher than the case 2 in the Table 1, which produced 1.5A cm^{-2} at 1.6 V, given the minor impact of reduced catalyst loading cost on the current overall system cost. Considering the future large impact of catalysts on the overall cost, this scenario must be changed. Therefore, to fulfill the critical value of Ir–PD and to simultaneously bring down the cost of green H_2 to the level of or below that of grey H_2, the most viable measures in the near future are the reduction in catalyst loading, the energy cost, and the cost of Ti-bipolar plates and PTLs. The widespread development of renewable energy and electrolysis-dedicated renewable energy plants are foreseeable in the near future, which will significantly decrease the energy cost for H_2 production. The Ti material of bipolar plates could be possibly replaced by stainless steel if appropriate protective layers are developed by coating with, for example, a thin gold layer.[144] The reduction in bipolar plate cost alone could reduce the overall cost of the system by 55% as estimated by Ayers et. al.[9] We envisage that all these factors, combined with the economy of scale effect, will decrease the green H_2 production cost to a value lower than 1.77 €/ kgH_2 (the lowest value in Table 1). Consequently, the gigawatt-scale deployment of PEMWE for green H_2 production with cost effectiveness (comparable with or even lower than grey H_2) is foreseeable in the near future.

4. Membrane

As mentioned in 2. Fundamentals for Development of PEMWE, the membrane is a central component, performing a dual functionality: the separation of the produced H_2 and O_2 gases and the transfer of protons between the electrodes to close the operational circuit. Thus, the membrane plays a big role in the safety operation and energy efficiency of the device as well as the purity of H_2 gas product. To ensure low gas crossover, commercial PEMWEs use relatively thick Nafion membranes such as Nafion 115 (127 μm thick) or Nafion 117 (178 μm thick), compared to conventional fuel cell with membrane thickness usually of ≈20–50 μm. According to the data in Figure 2, the ohmic loss linearly increases with current density. Indeed, at 2.5 A cm^{-2}, it exceeds the kinetic loss and becomes the major loss component within higher current density area. Given that the membrane resistance accounts for the majority (≈80%) of ohmic resistance, the membrane voltage loss dominates the overall cell voltage losses at high current density operation.[16] Holzapfel et. al.[133] showed that the use of a thin membrane (60 μm thick) significantly decreased voltage losses, and increased the current density by factor of two at 1.8 V, compared to a cell with a thicker membrane (i.e., ≈200 μm Nafion 117). Using a thin membrane however raises safety issues due to high H_2 crossover to the O_2 compartment of the anode. This might lead to crossed over H_2 content exceeding the upper limit of 4 vol% of O_2 gas (flammability limit), especially at low current density operation.[146,147] Babic et. al.[10] calculated operational current density range of PEMWEs using membranes with different thicknesses of 30 μm, 60 μm, and 180 μm, operated at 80 °C

under balanced pressure of 30 bar. The upper current density limit (i_{max}) was set by voltage of 2 V, whereas the lower limit (i_{min}) was set by 2 vol% crossover H_2 in O_2 gas. The operational current ranges were determined as ($i_{min,}$ A cm^{-2}; $i_{max,}$ A cm^{-2}) = (6.10; 7.07), (3.05; 5.21), and (0.91; 2.36) for the cells with membrane thickness of 30, 60, and 180 µm, respectively. Therefore, thinner membranes largely restricted the lower limit of operational current ranges. For the 60 µm case, i_{min} = 3.05 A cm^{-2} is obtained at ≈1.82 V, which exceeds the critical voltage in Table 2. Therefore, although thinner membranes drastically decrease the voltage loss, the high H_2 crossover restricts the operational range to the higher voltage range than critical value. To mitigate this effect, recombination catalysts can be implemented to reduce the crossover H_2 concentration at the anode. A small amount of Pt nanoparticles was introduced into the membrane to catalyze the recombination of O_2 and H_2 to H_2O within the membrane. This strategy was shown to neutralize almost all the H_2 crossovers at ambient conditions.[148] In a different study, the strategy which was applied under higher pressures up to 10 bar, also yielded very good results.[149] Also, to avoid the influence of the catalysts on the membrane performance, additional recombination catalysts are sometimes implemented into the anodic catalyst layers.[150] For example, the implementation of PtCo alloy particles into the anode showed a promising result of eliminating 99.5% of crossover H_2 content in O_2 gas.[150] This allowed cell operation with 90µm-thick membrane at current density as low as 0.15 A cm^{-2} under 20 bar difference pressure, while still maintaining crossover H_2 content lower than flammability limit. These promising results suggest that such approaches could be utilized in the future to make the use of thin membrane feasible for a larger operational current range. Additionally, there are widespread works on novel membrane materials other than Nafion, for example, novel ionic conducting polymers such as sulfonated poly(arylene ether sulfone) or sulfonated poly(phenylene sulfone) with high ionic conductivity and low gas permeability have been developed and deployed for PEMWE.[151,152] This membrane class showed high conductivity and low gas crossover. However, the mechanical and chemical long term stability still needs to be improved. However, a full review of all possible materials systems is beyond the scope of this review. Therefore, for more information concerning polymer membrane materials, the readers are referred to a recent review.[153]

5. Conclusions and Perspectives

Extensive knowledge about the structures of catalyst layers and electrodes for PEMWE has been gained and reported so far with really exciting results in the last few years. Still, bringing together different fragments of all these approaches into a coherent strategy is a target to be fulfilled. The different strategies have the potential to aid the design of the next generation of efficient catalysts and catalyst layers. In PEMWEs, the relation between catalysts and transport cannot be thought independently from each other but must be tailored into a holistic concept. Various Ir and Ru based catalyst forms have been developed and successfully implemented in full cell PEMWEs. Supported Ir oxide catalysts are proven to have an improved dispersion and show promising performance with respect to both activity and stability at low loadings. We emphasize the importance of low packing density of a catalyst, described by the thickness factor, µm (mg_{Ir} cm^{-2})$^{-1}$, for the design of new structural catalysts. A higher thickness factor often results in higher catalyst utilization; as the class of catalysts with high thickness factor such as RSDT, NSTF, and NWs, 3D printed CLs have shown outstanding activities at loadings lower than 0.3 mg cm^{-2}.

For the design of an optimum anodic electrode especially with low Ir-loading, the crucial parameters, including ionomer content of the catalyst layer, porosity, interfacial contact between catalyst layers and Ti-porous layers as well as the electrical conductivity of the catalyst layers are needed to be taken into account. The optimum ionomer content in wt% of a catalyst layer is specified for a specific catalyst. It should be therefore investigated when developing any catalyst layers using a new catalyst. The optimal ionomer content in vol% is however in a range of 30 vol%. Porosity of a catalyst layer is a decisive factor that should be accounting for about >30 vol% of catalyst layer volume for facilitating any mass transport phenomena during the cell operation. The interfacial resistance makes a significant contribution to the cell HFR if low loading catalyst layers are used. Thus, strategies such as developing PTE-based MEA configuration or implementation of a MPL to increase the interfacial area are the viable ways to accomplish electrodes with low loadings.

The critical parameters introduced in this review aim to set the standards for research and development to successfully achieve the large market penetration of PEMWE technology. From the best of our knowledge, only one publication has reported so far a cell performance which exceeds the requirement of critical iridium specific power (Ir–SP) of 50 kW g_{Ir}^{-1}.[101] However, it failed to meet the requirement of cell activity of ≥1 A cm^{-2} at 1.6 V, and no stability data were shown. The result is nevertheless encouraging as it proves at least that an Ir-based catalyst is sufficient in terms of resource availability. In order for PEMWEs to penetrate the world market at GW scale, it is clear that research and development toward low loadings in anodic catalyst layers and cost reduction of the bipolar plates and porous transport layers are the most viable approaches. This should particularly focus on concerted approaches from catalyst to single cell design to achieve a sufficient cell activity and stability at the lowest catalyst loading possible.

Acknowledgements

The authors gratefully acknowledge the financial support by the Federal Ministry of Education and Research of Germany in the framework of StacIE project (03HY103H). S.C. and D.E.L. thank the DFG for financial support within the grant CH 1763/3-1 as part of the Priority Program SPP 2080 "Catalysts and reactors under dynamic conditions for energy storage and conversion." S.C. also thanks the DFG for financial support within the grant CH 1763/4-1.

Open access funding enabled and organized by Projekt DEAL.

Conflict of Interest

The authors declare no conflict of interest.

Keywords

catalyst layers, electrocatalysis, electrode design, hydrogen production, membrane electrode assembly, oxygen evolution reaction, PEM water electrolyzers

Received: June 30, 2021
Revised: August 30, 2021
Published online: October 13, 2021

[1] Levelized Cost of Energy and Levelized Cost of Storage, https://www.lazard.com/perspective/lcoe2019 (accessed: November 2020).
[2] B. Pivovar, N. Rustagi, S. Satyapal, *Electrochem. Soc. Interface* **2018**, *27*, 47.
[3] R. Clémençon, *J. Environ. Dev.* **2016**, *25*, 3.
[4] O. Schmidt, A. Gambhir, I. Staffell, A. Hawkes, J. Nelson, S. Few, *Int. J. Hydrogen Energy* **2017**, *42*, 30470.
[5] S. Shiva Kumar, V. Himabindu, *Mater. Sci. Energy Technol.* **2019**, *2*, 442.
[6] M. Bernt, A. Hartig-Weiß, M. F. Tovini, H. A. El-Sayed, C. Schramm, J. Schröter, C. Gebauer, H. A. Gasteiger, *Chem. Ing. Tech.* **2019**, *92*, 31.
[7] M. S. Cha, J. E. Park, S. Kim, S.-H. Han, S.-H. Shin, S. H. Yang, T.-H. Kim, D. M. Yu, S. So, Y. T. Hong, S. J. Yoon, S.-G. Oh, S. Y. Kang, O.-H. Kim, H. S. Park, B. Bae, Y.-E. Sung, Y.-H. Cho, J. Y. Lee, *Energy Environ. Sci.* **2020**, *13*, 3633.
[8] D. Li, E. J. Park, W. Zhu, Q. Shi, Y. Zhou, H. Tian, Y. Lin, A. Serov, B. Zulevi, E. D. Baca, C. Fujimoto, H. T. Chung, Y. S. Kim, *Nat. Energy* **2020**, *31*, 1805876.
[9] K. Ayers, N. Danilovic, R. Ouimet, M. Carmo, B. Pivovar, M. Bornstein, *Annu. Rev. Chem. Biomol. Eng.* **2019**, *10*, 219.
[10] U. Babic, M. Suermann, F. N. Büchi, L. Gubler, T. J. Schmidt, *J. Electrochem. Soc.* **2017**, *164*, F387.
[11] The clean hydrogen future has already begun – Analysis – IEA, https://www.iea.org/commentaries/the-clean-hydrogen-future-has-already-begun (accessed: November 2020).
[12] International Energy Agency (IEA) – Clingendael International Energy Programme (CIEP), https://iea.blob.core.windows.net/assets/ccbc3b01-7403-4c15-90a2-af11dfb92c62/Hydrogen_in_North_Western_Europe.pdf (accessed: August 2021).
[13] International Energy Agency- IEA, https://iea.blob.core.windows.net/assets/9e3a3493-b9a6-4b7d-b499-7ca48e357561/The_Future_of_Hydrogen.pdf.
[14] C. Minke, M. Suermann, B. Bensmann, R. Hanke-Rauschenbach, *Int. J. Hydrogen Energy* **2021**, *46*, 23581.
[15] M. Bernt, A. Siebel, H. A. Gasteiger, *J. Electrochem. Soc.* **2018**, *165*, F305.
[16] M. Bernt, H. A. Gasteiger, *J. Electrochem. Soc.* **2016**, *163*, F3179.
[17] H.-S. Oh, H. N. Nong, P. Strasser, *Adv. Funct. Mater.* **2015**, *25*, 1074.
[18] S. Maass, F. Finsterwalder, G. Frank, R. Hartmann, C. Merten, *J. Power Sources* **2008**, *176*, 444.
[19] Y. Yi, G. Weinberg, M. Prenzel, M. Greiner, S. Heumann, S. Becker, R. Schlögl, *Catal. Today* **2017**, *295*, 32.
[20] O. Kasian, T. Li, A. M. Mingers, K. Schweinar, A. Savan, A. Ludwig, K. J. Mayrhofer, *J. Phys. Energy* **2020**, *3*, 034006.
[21] F. Hegge, F. Lombeck, E. Cruz Ortiz, L. Bohn, M. von Holst, M. Kroschel, J. Hübner, M. Breitwieser, P. Strasser, S. Vierrath, *ACS Appl. Energy Mater.* **2020**, *3*, 8276.
[22] T. Schuler, T. J. Schmidt, F. N. Büchi, *J. Electrochem. Soc.* **2019**, *166*, F555.
[23] B. J. Etzold, U. Krewer, S. Thiele, A. Dreizler, E. Klemm, T. Turek, *Chem. Eng. J.* **2021**, *424*, 130501.
[24] M. Suermann, T. J. Schmidt, F. N. Büchi, *Electrochim. Acta* **2016**, *211*, 989.
[25] S. G. Bratsch, *J. Phys. Chem. Ref. Data* **1989**, *18*, 1.
[26] Levelized Cost of Energy, Levelized Cost of Storage, and Levelized Cost of Hydrogen, https://www.lazard.com/perspective/levelized-cost-of-energy-levelized-cost-of-storage-and-levelized-cost-of-hydrogen/ (accessed: August 2021).
[27] DOE Technical Targets for Hydrogen Production from Electrolysis, https://www.energy.gov/eere/fuelcells/doe-technical-targets-hydrogen-production-electrolysis (accessed: February 2021).
[28] A. R. Zeradjanin, A. Vimalanandan, G. Polymeros, A. A. Topalov, Mayrhofer, J. J. Karl, M. Rohwerder, *Phys.Chem.Chem. Phys.* **2017**, *19*, 17019.
[29] H. N. Nong, L. J. Falling, A. Bergmann, M. Klingenhof, H. P. Tran, C. Spöri, R. Mom, J. Timoshenko, G. Zichittella, A. Knop-Gericke, S. Piccinin, J. Pérez-Ramírez, B. R. Cuenya, R. Schlögl, P. Strasser, D. Teschner, T. E. Jones, *Nature* **2020**, *587*, 408.
[30] R. Adams, R. L. Shriner, *J. Am. Chem. Soc.* **1923**, *45*, 2171.
[31] M. Carmo, D. L. Fritz, J. Mergel, D. Stolten, *Int. J. Hydrogen Energy* **2013**, *38*, 4901.
[32] S. Siracusano, N. van Dijk, E. Payne-Johnson, V. Baglio, A. S. Aricò, *Appl. Catal., B* **2015**, *164*, 488.
[33] N. Mamaca, E. Mayousse, S. Arrii-Clacens, T. W. Napporn, K. Servat, N. Guillet, K. B. Kokoh, *Appl. Catal., B* **2012**, *111*, 376.
[34] G. C. da Silva, N. Perini, E. A. Ticianelli, *Appl. Catal., B* **2017**, *218*, *287*.
[35] T. Audichon, E. Mayousse, S. Morisset, C. Morais, C. Comminges, T. W. Napporn, K. B. Kokoh, *Int. J. Hydrogen Energy* **2014**, *39*, 16785.
[36] R. E. Fuentes, J. Farell, J. W. Weidner, *Electrochem. Solid-State Lett.* **2011**, *14*, E5.
[37] J. M. Roller, S. Kim, T. Kwak, H. Yu, R. Maric, *J. Mater. Sci.* **2017**, *52*, 9391.
[38] H. Yu, N. Danilovic, Y. Wang, W. Willis, A. Poozhikunnath, L. Bonville, C. Capuano, K. Ayers, R. Maric, *Appl. Catal., B* **2018**, *239*, 133.
[39] D. Escalera-López, S. Czioska, J. Geppert, A. Boubnov, P. Röse, E. Saraçi, U. Krewer, J.-D. Grunwaldt, S. Cherevko, *ACS Catal.* **2021**, *11*, 9300.
[40] S. Czioska, A. Boubnov, D. Escalera-López, J. Geppert, A. Zagalskaya, P. Röse, E. Saraçi, V. Alexandrov, U. Krewer, S. Cherevko, J.-D. Grunwaldt, *ACS Catal.* **2021**, *11*, 10043.
[41] T. J. Schmidt, H. A. Gasteiger, G. D. Stäb, P. M. Urban, D. M. Kolb, R. J. Behm, *J. Electrochem. Soc.* **1998**, *145*, 2354.
[42] U. A. Paulus, T. J. Schmidt, H. A. Gasteiger, R. J. Behm, *J. Electroanal. Chem.* **2001**, *495*, 134.
[43] C. C. L. McCrory, S. Jung, I. M. Ferrer, S. M. Chatman, J. C. Peters, T. F. Jaramillo, *J. Am. Chem. Soc.* **2015**, *137*, 4347.
[44] C. Wei, R. R. Rao, J. Peng, B. Huang, I. E. L. Stephens, M. Risch, Z. J. Xu, Y. Shao-Horn, *Adv. Mater.* **2019**, *31*, 1806296.
[45] C. H. Bamford, C. F. H. Tipper, R. G. Compton, in *Electrode Kinetics: Principles and Methodology*, Comprehensive Chemical Kinetics (Eds: C. H. Bramford, R. G. Compton), Vol. *26*, Elsevier, Burlington, MA **1986**.
[46] W. T. Hong, M. Risch, K. A. Stoerzinger, A. Grimaud, J. Suntivich, Y. Shao-Horn, *Energy Environ. Sci.* **2015**, *8*, 1404.
[47] S. Anantharaj, S. Noda, M. Driess, P. W. Menezes, *ACS Energy Lett.* **2021**, *6*, 1607.
[48] D. Y. Chung, S. Park, P. P. Lopes, V. R. Stamenkovic, Y.-E. Sung, N. M. Markovic, D. Strmcnik, *ACS Catal.* **2020**, *10*, 4990.
[49] V. Čolić, J. Tymoczko, A. Maljusch, A. Ganassin, W. Schuhmann, A. S. Bandarenka, *ChemElectroChem* **2015**, *2*, 143.
[50] T. Bligaard, R. M. Bullock, C. T. Campbell, J. G. Chen, B. C. Gates, R. J. Gorte, C. W. Jones, W. D. Jones, J. R. Kitchin, S. L. Scott, *ACS Catal.* **2016**, *6*, 2590.
[51] S. M. Alia, K. E. Hurst, S. S. Kocha, B. S. Pivovar, *J. Electrochem. Soc.* **2016**, *163*, F3051.

[52] S. Watzele, P. Hauenstein, Y. Liang, S. Xue, J. Fichtner, B. Garlyyev, D. Scieszka, F. Claudel, F. Maillard, A. S. Bandarenka, *ACS Catal.* **2019**, *9*, 9222.
[53] S. Watzele, A. S. Bandarenka, *Electroanalysis* **2016**, *28*, 2394.
[54] S. Geiger, O. Kasian, A. M. Mingers, S. S. Nicley, K. Haenen, K. J. J. Mayrhofer, S. Cherevko, *ChemSusChem* **2017**, *10*, 4140.
[55] S. Geiger, O. Kasian, M. Ledendecker, E. Pizzutilo, A. M. Mingers, W. T. Fu, O. Diaz-Morales, Z. Li, T. Oellers, L. Fruchter, A. Ludwig, Mayrhofer, J. J. Karl, M. T. M. Koper, S. Cherevko, *Nat. Catal.* **2018**, *1*, 508.
[56] S. M. Alia, S. Stariha, R. L. Borup, *J. Electrochem. Soc.* **2019**, *166*, F11642.
[57] J. Knöppel, M. Möckl, D. Escalera-López, K. Stojanovski, M. Bierling, T. Böhm, S. Thiele, M. Rzepka, S. Cherevko, *Nat. Commun.* **2021**, *12*, 2231.
[58] C. Spöri, J. T. H. Kwan, A. Bonakdarpour, D. P. Wilkinson, P. Strasser, *Angew. Chem., Int. Ed.* **2017**, *56*, 5994.
[59] H. A. El-Sayed, A. Weiß, L. F. Olbrich, G. P. Putro, H. A. Gasteiger, *J. Electrochem. Soc.* **2019**, *166*, F458.
[60] A. Hartig-Weiss, M. F. Tovini, H. A. Gasteiger, H. A. El-Sayed, *ACS Appl. Energy Mater.* **2020**, *3*, 10323.
[61] M. Fathi Tovini, A. Hartig-Weiß, H. A. Gasteiger, H. A. El-Sayed, *J. Electrochem. Soc.* **2021**, *168*, 014512.
[62] R. Frydendal, E. A. Paoli, B. P. Knudsen, B. Wickman, P. Malacrida, I. E. L. Stephens, I. Chorkendorff, *ChemElectroChem* **2014**, *1*, 2075.
[63] J. Kibsgaard, I. Chorkendorff, *Nat. Energy* **2019**, *355*, 146.
[64] S. ABBOU, R. Chattot, V. Martin, F. Claudel, L. Solà-Hernandez, C. Beauger, L. Dubau, F. Maillard, *ACS Catal.* **2020**, *10*, 7283.
[65] C. Da Daiane Ferreira Silva, F. Claudel, V. Martin, R. Chattot, S. ABBOU, K. Kumar, I. Jiménez-Morales, S. Cavaliere, D. Jones, J. Rozière, L. Solà-Hernandez, C. Beauger, M. Faustini, J. Peron, B. Gilles, T. Encinas, L. Piccolo, F. H. Barros de Lima, L. Dubau, F. Maillard, *ACS Catal.* **2021**, *11*, 4107.
[66] C. van Pham, M. Bühler, J. Knöppel, M. Bierling, D. Seeberger, D. Escalera-López, K. J. Mayrhofer, S. Cherevko, S. Thiele, *Appl. Catal., B* **2020**, *269*, 118762.
[67] P. K. R. Holzapfel, M. Bühler, D. Escalera-López, M. Bierling, F. D. Speck, Mayrhofer, J. J. Karl, S. Cherevko, C. V. Pham, S. Thiele, *Small* **2020**, *16*, 2003161.
[68] M. A. Hubert, A. M. Patel, A. Gallo, Y. Liu, E. Valle, M. Ben-Naim, J. Sanchez, D. Sokaras, R. Sinclair, J. K. Nørskov, L. A. King, M. Bajdich, T. F. Jaramillo, *ACS Catal.* **2020**, *10*, 12182.
[69] Y. Chen, H. Li, J. Wang, Y. Du, S. Xi, Y. Sun, M. Sherburne, J. W. Ager, A. C. Fisher, Z. J. Xu, *Nat. Commun.* **2019**, *10*, 572.
[70] J. G. Vos, Z. Liu, F. D. Speck, N. Perini, W. Fu, S. Cherevko, M. T. M. Koper, *ACS Catal.* **2019**, *9*, 8561.
[71] S. M. Alia, M.-A. Ha, G. C. Anderson, C. Ngo, S. Pylypenko, R. E. Larsen, *J. Electrochem. Soc.* **2019**, *166*, F1243.
[72] K. Ehelebe, D. Escalera-López, S. Cherevko, *Curr. Opin. Electrochem.* **2021**, *29*, 100832.
[73] M. Suermann, B. Bensmann, R. Hanke-Rauschenbach, *J. Electrochem. Soc.* **2019**, *166*, F645.
[74] M. Suermann, T. J. Schmidt, F. N. Büchi, *Electrochim. Acta* **2018**, *281*, 466.
[75] G. Bender, M. Carmo, T. Smolinka, A. Gago, N. Danilovic, M. Mueller, F. Ganci, A. Fallisch, P. Lettenmeier, K. A. Friedrich, K. Ayers, B. Pivovar, J. Mergel, D. Stolten, *Int. J. Hydrogen Energy* **2019**, *44*, 9174.
[76] C. Spöri, C. Brand, M. Kroschel, P. Strasser, *J. Electrochem. Soc.* **2021**, *168*, 034508.
[77] P. Aßmann, A. S. Gago, P. Gazdzicki, K. A. Friedrich, M. Wark, *Curr. Opin. Electrochem.* **2020**, *21*, 225.
[78] C. Rozain, E. Mayousse, N. Guillet, P. Millet, *Appl. Catal., B* **2016**, *182*, 153.
[79] J. Lopata, Z. Kang, J. Young, G. Bender, J. W. Weidner, S. Shimpalee, *J. Electrochem. Soc.* **2020**, *167*, 064507.
[80] C. Rozain, E. Mayousse, N. Guillet, P. Millet, *Appl. Catal., B* **2016**, *182*, 123.
[81] S. Siracusano, V. Baglio, N. van Dijk, L. Merlo, A. S. Aricò, *Appl. Energy* **2017**, *192*, 477.
[82] S. Siracusano, N. Hodnik, P. Jovanovic, F. Ruiz-Zepeda, M. Šala, V. Baglio, A. S. Aricò, *Nano Energy* **2017**, *40*, 618.
[83] S. Cherevko, S. Geiger, O. Kasian, N. Kulyk, J.-P. Grote, A. Savan, B. R. Shrestha, S. Merzlikin, B. Breitbach, A. Ludwig, K. J. Mayrhofer, *Catal. Today* **2016**, *262*, 170.
[84] O. Kasian, J.-P. Grote, S. Geiger, S. Cherevko, K. J. J. Mayrhofer, *Angew. Chem., Int. Ed.* **2018**, *57*, 2488.
[85] H. Yu, L. Bonville, J. Jankovic, R. Maric, *Appl. Catal., B* **2020**, *260*, 118194.
[86] C. Rakousky, U. Reimer, K. Wippermann, M. Carmo, W. Lueke, D. Stolten, *J. Power Sources* **2016**, *326*, 120.
[87] Q. Feng, X. Yuan, G. Liu, B. Wei, Z. Zhang, H. Li, H. Wang, *J. Power Sources* **2017**, *366*, 33.
[88] A. Weiß, A. Siebel, M. Bernt, T.-H. Shen, V. Tileli, H. A. Gasteiger, *J. Electrochem. Soc.* **2019**, *166*, F487.
[89] D. F. Abbott, D. Lebedev, K. Waltar, M. Povia, M. Nachtegaal, E. Fabbri, C. Copéret, T. J. Schmidt, *Chem. Mater.* **2016**, *28*, 6591.
[90] V. Streibel, M. Hävecker, Y. Yi, J. J. Velasco Vélez, K. Skorupska, E. Stotz, A. Knop-Gericke, R. Schlögl, R. Arrigo, *Top. Catal.* **2018**, *61*, 2064.
[91] J. M. Yoo, H. Shin, S. Park, Y.-E. Sung, *J. Phys. D: Appl. Phys.* **2021**, *54*, 173001.
[92] Z. Kang, S. M. Alia, M. Carmo, G. Bender, *J. Power Sources* **2021**, *481*, 229012.
[93] E. Brightman, J. Dodwell, N. van Dijk, G. Hinds, *Electrochem. Commun.* **2015**, *52*, 1.
[94] H. Becker, L. Castanheira, G. Hinds, *J. Power Sources* **2020**, *448*, 227563.
[95] J. Dodwell, M. Maier, J. Majasan, R. Jervis, L. Castanheira, P. Shearing, G. Hinds, D. Brett, *J. Power Sources* **2021**, *498*, 229937.
[96] U. Babic, M. Tarik, T. J. Schmidt, L. Gubler, *J. Power Sources* **2020**, *451*, 227778.
[97] L. J. Nuttall, A. P. Fickett, W. A. Titterington, in *Hydrogen Energy* (Ed.: T. N. Veziroğlu), Springer Verlag, Boston, MA **2012**, p. 441.
[98] J. H. Russell, L. J. Nuttall, A. P. Fickett, *Prepr. Pap. - Am. Chem. Soc., Div. Fuel Chem.* **1973**, *18*, 24.
[99] M. Yamaguchi, K. Okisawa, T. Nakanori, in *Intersociety Conf. on Energy Conversion Engineering (IECEC)*, IEEE, Piscataway, NJ **1997**.
[100] M. Bühler, F. Hegge, P. Holzapfel, M. Bierling, M. Suermann, S. Vierrath, S. Thiele, *J. Mater. Chem. A* **2019**, *165*, F305.
[101] Z. Taie, X. Peng, D. Kulkarni, I. V. Zenyuk, A. Z. Weber, C. Hagen, N. Danilovic, *ACS Appl. Mater. Interfaces* **2020**, *12*, 52701.
[102] F. Hegge, R. Moroni, P. Trinke, B. Bensmann, R. Hanke-Rauschenbach, S. Thiele, S. Vierrath, *J. Power Sources* **2018**, *393*, 62.
[103] H. Su, V. Linkov, B. J. Bladergroen, *Int. J. Hydrogen Energy* **2013**, *38*, 9601.
[104] E. Oakton, D. Lebedev, A. Fedorov, F. Krumeich, J. Tillier, O. Sereda, T. J. Schmidt, C. Copéret, *New J. Chem.* **2016**, *40*, 1834.
[105] E. Oakton, D. Lebedev, M. Povia, D. F. Abbott, E. Fabbri, A. Fedorov, M. Nachtegaal, C. Copéret, T. J. Schmidt, *ACS Catal.* **2017**, *7*, 2346.
[106] P. Mazúr, J. Polonský, M. Paidar, K. Bouzek, *Int. J. Hydrogen Energy* **2012**, *37*, 12081.
[107] H. Lv, S. Wang, C. Hao, W. Zhou, J. Li, M. Xue, C. Zhang, *ChemCatChem* **2019**, *11*, 2511.
[108] C. Hao, H. Lv, C. Mi, Y. Song, J. Ma, *ACS Sustainable Chem. Eng.* **2015**, *4*, 746.
[109] C. Hao, H. Lv, Q. Zhao, B. Li, C. Zhang, C. Mi, Y. Song, J. Ma, *Int. J. Hydrogen Energy* **2017**, *42*, 9384.

[110] S. Zhao, A. Stocks, B. Rasimick, K. More, H. Xu, *J. Electrochem. Soc.* **2018**, *165*, F82.
[111] H. Ohno, S. Nohara, K. Kakinuma, M. Uchida, H. Uchida, *Catalysts* **2019**, *9*, 74.
[112] G. C. Silva, S. I. Venturini, S. Zhang, M. Löffler, C. Scheu, Mayrhofer, J. J. Karl, E. A. Ticianelli, S. Cherevko, *ChemElectroChem* **2020**, *7*, 2330.
[113] S. Geiger, O. Kasian, A. M. Mingers, Mayrhofer, J. J. Karl, S. Cherevko, *Sci. Rep.* **2017**, *7*, 4595.
[114] K. E. Ayers, J. N. Renner, N. Danilovic, J. X. Wang, Y. Zhang, R. Maric, H. Yu, *Catal. Today* **2016**, *262*, 121.
[115] L. Nereng, in *1st International Conference on Electrolysis*, ICE2017, Copenhagen **2017**.
[116] M. K. Debe, *ECS Trans.* **2012**, *45*, 47.
[117] K. A. Lewinski, S. M. Luopa, F. Sun, C. Jentzsch, D. Franciscus van der Vliet, *ECS Meeting Abstracts* **2018**, *MA2018-01*, 1637.
[118] T. Audichon, E. Mayousse, T. W. Napporn, C. Morais, C. Comminges, K. B. Kokoh, *Electrochim. Acta* **2014**, *132*, 284.
[119] S. Siracusano, V. Baglio, E. Moukheiber, L. Merlo, A. S. Aricò, *Int. J. Hydrogen Energy* **2015**, *40*, 14430.
[120] F. Pantò, S. Siracusano, N. Briguglio, A. S. Aricò, *Appl. Energy* **2020**, *279*, 115809.
[121] H. N. Nong, L. Gan, E. Willinger, D. Teschner, P. Strasser, *Chem. Sci.* **2014**, *5*, 2955.
[122] H. N. Nong, T. Reier, H.-S. Oh, M. Gliech, P. Paciok, T. H. T. Vu, D. Teschner, M. Heggen, V. Petkov, R. Schlögl, T. Jones, P. Strasser, *Nat. Catal.* **2018**, *1*, 841.
[123] S. M. Alia, S. Shulda, C. Ngo, S. Pylypenko, B. S. Pivovar, *ACS Catal.* **2018**, *8*, 2111.
[124] M. Huynh, C. Shi, S. J. L. Billinge, D. G. Nocera, *J. Am. Chem. Soc.* **2015**, *137*, 14887.
[125] A. Li, H. Ooka, N. Bonnet, T. Hayashi, Y. Sun, Q. Jiang, C. Li, H. Han, R. Nakamura, *Angew. Chem., Int. Ed.* **2019**, *58*, 5054.
[126] M. Chatti, J. L. Gardiner, M. Fournier, B. Johannessen, T. Williams, T. R. Gengenbach, N. Pai, C. Nguyen, D. R. MacFarlane, R. K. Hocking, A. N. Simonov, *Nat. Catal.* **2019**, *2*, 457.
[127] L. C. Seitz, C. F. Dickens, K. Nishio, Y. Hikita, J. Montoya, A. Doyle, C. Kirk, A. Vojvodic, H. Y. Hwang, J. K. Norskov, T. F. Jaramillo, *Science* **2016**, *353*, 1011.
[128] B.-J. Kim, D. F. Abbott, X. Cheng, E. Fabbri, M. Nachtegaal, F. Bozza, I. E. Castelli, D. Lebedev, R. Schäublin, C. Copéret, T. Graule, N. Marzari, T. J. Schmidt, *ACS Catal.* **2017**, *7*, 3245.
[129] Y. Lin, Z. Tian, L. Zhang, J. Ma, Z. Jiang, B. J. Deibert, R. Ge, L. Chen, *Nat. Commun.* **2019**, *10*, 162.
[130] J. Mo, Z. Kang, S. T. Retterer, D. A. Cullen, T. J. Toops, J. B. Green, M. M. Mench, F.-Y. Zhang, *Sci. Adv.* **2016**, *2*, e1600690.
[131] C. Liu, M. Shviro, A. S. Gago, S. F. Zaccarine, G. Bender, P. Gazdzicki, T. Morawietz, I. Biswas, M. Rasinski, A. Everwand, R. Schierholz, J. Pfeilsticker, M. Müller, P. P. Lopes, R.-A. Eichel, B. Pivovar, S. Pylypenko, K. A. Friedrich, W. Lehnert, M. Carmo, *Adv. Energy Mater.* **2021**, *11*, 2002926.
[132] M. Bühler, P. Holzapfel, D. McLaughlin, S. Thiele, *J. Electrochem. Soc.* **2019**, *166*, F1070.
[133] P. Holzapfel, M. Bühler, C. van Pham, F. Hegge, T. Böhm, D. McLaughlin, M. Breitwieser, S. Thiele, *Electrochem. Commun.* **2020**, *110*, 106640.
[134] A. Hartig-Weiss, M. Miller, H. Beyer, A. Schmitt, A. Siebel, A. T. S. Freiberg, H. A. Gasteiger, H. A. El-Sayed, *ACS Appl. Nano Mater.* **2020**, *3*, 2185.
[135] B.-S. Lee, S. H. Ahn, H.-Y. Park, I. Choi, S. J. Yoo, H.-J. Kim, D. Henkensmeier, J. Y. Kim, S. Park, S. W. Nam, K.-Y. Lee, J. H. Jang, *Appl. Catal., B* **2015**, *179*, 285.
[136] H. Kim, J. Kim, J. Kim, G. H. Han, W. Guo, S. Hong, H. S. Park, H. W. Jang, S. Y. Kim, S. H. Ahn, *Appl. Catal., B* **2021**, *283*, 119596.
[137] S. Choe, B.-S. Lee, M. K. Cho, H.-J. Kim, D. Henkensmeier, S. J. Yoo, J. Y. Kim, S. Y. Lee, H. S. Park, J. H. Jang, *Appl. Catal., B* **2018**, *226*, 289.
[138] A. Lim, J. Kim, H. J. Lee, H.-J. Kim, S. J. Yoo, J. H. Jang, H. Young Park, Y.-E. Sung, H. S. Park, *Appl. Catal., B* **2020**, *272*, 118955.
[139] Z. Kang, J. Mo, G. Yang, S. T. Retterer, D. A. Cullen, T. J. Toops, J. B. Green Jr, M. M. Mench, F.-Y. Zhang, *Energy Environ. Sci.* **2017**, *10*, 166.
[140] Z. Kang, G. Yang, J. Mo, S. Yu, D. A. Cullen, S. T. Retterer, T. J. Toops, M. P. Brady, G. Bender, B. S. Pivovar, J. B. Green, F.-Y. Zhang, *Int. J. Hydrogen Energy* **2018**, *43*, 14618.
[141] P. Lettenmeier, S. Kolb, N. Sata, A. Fallisch, L. Zielke, S. Thiele, A. S. Gago, K. A. Friedrich, *Energy Environ. Sci.* **2017**, *38*, 4901.
[142] T. Schuler, J. M. Ciccone, B. Krentscher, F. Marone, C. Peter, T. J. Schmidt, F. N. Büchi, *Adv. Energy Mater.* **2019**, *10*, 1903216.
[143] S. Siracusano, A. Di Blasi, V. Baglio, G. Brunaccini, N. Briguglio, A. Stassi, R. Ornelas, E. Trifoni, V. Antonucci, A. S. Aricò, *Int J Hydrogen Energy* **2011**, *36*, 3333.
[144] G. Yang, S. Yu, J. Mo, Z. Kang, Y. Dohrmann, F. A. List, J. B. Green, S. S. Babu, F.-Y. Zhang, *J. Power Sources* **2018**, *396*, 590.
[145] Y. J. Kim, A. Lim, J. M. Kim, D. Lim, K. H. Chae, E. N. Cho, H. J. Han, K. U. Jeon, M. Kim, G. H. Lee, G. R. Lee, H. S. Ahn, H. S. Park, H. Kim, J. Y. Kim, Y. S. Jung, *Nat. Commun.* **2020**, *11*, 4921.
[146] P. Trinke, B. Bensmann, R. Hanke-Rauschenbach, *Int. J. Hydrogen Energy* **2017**, *42*, 14355.
[147] P. Trinke, B. Bensmann, R. Hanke-Rauschenbach, *Electrochem. Commun.* **2017**, *82*, 98.
[148] C. Klose, P. Trinke, T. Böhm, B. Bensmann, S. Vierrath, R. Hanke-Rauschenbach, S. Thiele, *J. Electrochem. Soc.* **2018**, *165*, F1271.
[149] S. Garbe, U. Babic, E. Nilsson, T. J. Schmidt, L. Gubler, *J. Electrochem. Soc.* **2019**, *166*, F873.
[150] N. Briguglio, S. Siracusano, G. Bonura, D. Sebastián, A. S. Aricò, *Appl. Catal., B* **2019**, *246*, 254.
[151] A. Daryaei, G. C. Miller, J. Willey, S. Roy Choudhury, B. Vondrasek, D. Kazerooni, M. R. Burtner, C. Mittelsteadt, J. J. Lesko, J. S. Riffle, J. E. McGrath, *ACS Appl. Mater. Interfaces* **2017**, *9*, 20067.
[152] C. Klose, T. Saatkamp, A. Münchinger, L. Bohn, G. Titvinidze, M. Breitwieser, K.-D. Kreuer, S. Vierrath, *Adv. Energy Mater.* **2020**, *10*, 1903995.
[153] Y. S. Kim, *ACS Appl. Polym. Mater.* **2021**, *3*, 1250.

Chuyen van Pham received his Ph.D. in 2015 from the University of Freiburg, Germany on the topic of synthesis, functionalization, and applications of graphene in energy conversion. He then worked as a postdoctoral researcher in electrochemical energy system group, the University of Freiburg on the development of electrocatalyst for PEM fuel cells and water electrolizers. Since January, 2021, he is a postdoctoral researcher in the Helmholtz Institute Erlangen-Nürnberg for Renewable Energy (HI-ERN), Germany. His research interests are the development of electrocatalysts for PEM fuel cells and water electrolyzers.

Daniel Escalera-López received in 2019, his Ph.D. with Integrated Studies in Fuel Cells and their Fuels from the University of Birmingham (United Kingdom), under the supervision of Dr. Neil V. Rees. Since 2019, he is a postdoctoral researcher in Electrochemical Energy Conversion team of Helmholtz Institute Erlangen–Nürnberg for Renewable Energy (HI-ERN), Germany. His current research involves the study of activity–stability relationships of noble and non-noble metal-based catalysts for electrochemical water splitting, by use of in situ and in operando coupled electrochemical and surface characterization techniques.

Karl Mayrhofer is since 2015, a professor of Electrocatalysis at the Friedrich–Alexander University Erlangen–Nuremberg, and the director of Helmholtz Institute Erlangen–Nürnberg for Renewable Energy, Germany. His research interests are electrochemical reactions in energy conversions (fuel cells, water or CO_2 electrolyzers etc.). Before these, he received his Ph.D. in 2005 from the Technische Universität Wien. He was a visiting researcher (2003–2005) in Lawrence Berkeley National Laboratory. After a 3 years' duration (2006–2009) as postoctoral at the Technische Universität München, Germany, he was a group leader (2010–2015) of the Max-Planck-Institut für Eisenforschung GmbH, Germany.

Serhiy Cherevko is a team head of the Electrochemical Energy Conversion group of the Helmholtz Institute Erlangen–Nürnberg for Renewable Energy (HI-ERN), Germany since 2016. His current research topics include fuel cells, water electrolysis, photo-electrochemistry, and noble metals recycling. Before this, he received his Ph.D. in 2009 in Nanoscience at the Sungkyunkwan University, South Korea. After working duration 2009–2011 as a Postdoctoral Research Fellow on chemical engineering, at Sungkyunkwan University, he worked 2011–2015 as postdoctoral Researcher in the department of Interface Chemistry and Surface Engineering, Max-Planck Institut für Eisenforschung, Germany.

Simon Thiele is since January, 2018, a professor for Electrocatalytical Interface Engineering at Friedrich–Alexander University Erlangen–Nuremberg, and the Head of Research Department, Electrocatalytic Interface Engineering, Helmholtz Institute Erlangen-Nurnberg for Renewable Energy (HI-ERN), Germany. Before this, he received his Ph.D. in 2013 on the topic of tomographic imaging, microstructure modeling, and reactant transport simulation on electrochemical energy conversion and storage devices. From 2011 to 2017, he was the group leader of an independent research group "Porous Media" at the University of Freiburg, focusing on electrochemical energy conversion systems, e.g. fuel cells or electrolyzers.